Taylor & Francis
Taylor & Francis Group

DEVELOPMENT OF A DISPERSION RELATION EQUATION – PRESERVING PURE ADVECTION SCHEME FOR SOLVING THE NAVIER-STOKES EQUATIONS WITH/WITHOUT FREE SURFACE

C. H. Yu[1,2] and Tony W. H. Sheu[1,3,4]

[1]*Department of Engineering Science and Ocean Engineering, National Taiwan University, Taipei, Taiwan, Republic of China*
[2]*Department of Ocean Science and Engineering, Zhejiang University, Hangzhou, Zhejiang, People's Republic of China*
[3]*Department of Mathematics, National Taiwan University, Taipei, Taiwan, Republic of China*
[4]*Taida Institute of Mathematical Science (TIMS), National Taiwan University, Taipei, Taiwan, Republic of China*

In this article we develop a dispersively more accurate pure advection scheme and apply it to properly simulate incompressible free surface flow equations. According to Clebsch velocity decomposition, the incompressible flow equations are decomposed into the equations accounting respectively for the flow potential, rotation, and dissipation. For the Euler equation, the midpoint implicit symplectic time integrator is applied to approximate the temporal derivative term. For the sake of reducing numerical dispersion error, the upwinding scheme is developed to minimize the difference between the numerical and exact dispersion relation equations for the time-dependent pure advection equation in wavenumber space.

1. INTRODUCTION

The inviscid Burgers' equation for modeling the transport of high-speed gas is one of the celebrated equations belonging to the class of Hamiltonian equations. When simulating this class of practically and scientifically important equations, it is essential to take its associated Hamiltonian properties into account using the symplectic numerical integrators to preserve the embedded symplecticity. The objective of this article is to develop a numerically stable and long-term accurate Euler flow solver. We will then apply it to simulate the incompressible viscous fluid flow investigated at high Reynolds number.

Simulation of the incompressible Navier-Stokes equations at high Reynolds numbers has been known to have many computational difficulties. One of the

Address correspondence to Tony W. H. Sheu, Department of Engineering Science and Ocean Engineering, National Taiwan University, No. 1, Sec. 4, Roosevelt Road, Taipei, Taiwan 106, Republic of China. E-mail: twhsheu@ntu.edu.tw

NOMENCLATURE

Cr	Courant number	Δx	grid spacing
$\underline{D}$	tensor defined in (38)	ε	Casimir functional
E	error function	θ	phase angle
Fr	Froude number defined in (38)	θ_e	Dirac delta function defined in (36)
G	amplification factor		
H	Hamiltonian functional	θ_e	exact phase angle
H^*	smoothed Heaviside function defined in (35)	κ	curvature
		λ^i	Clebsch variable
J	skew-symmetric transformation	μ	viscosity defined in (38)
k	wavenumber	μ^i	Clebsch variable
p	pressure defined in Eq. (1)	ρ	density defined in (38)
Re	Reynolds number	ϕ	field variable
$\underline{u}$	velocity vector defined in Eq. (1)	ψ	streamfunction
W	weighting function	ω	angular frequency
We	Weber number defined in (38)	$\tilde{\omega}$	vorticity
β	wave number	ω_{exact}	exact angular frequency
Δt	increment time	ω_{num}	numerical angular frequency

difficulties is associated with the approximation of the dominant nonlinear convection terms. Approximation of these spatial derivative terms needs to properly take their dispersive nature into consideration. How to reduce the difference between the exact and numerical dispersion relation equations motivates the current development of an upwinding scheme in wavenumber space. The other numerical instability problem encountered in incompressible flow simulation has relevance to approximation of the pressure gradient term in co-located grids. Suppression of these numerically generated unphysical even–odd (or checkerboard) oscillations in the pressure field motivated us to develop the center-type compact difference scheme to properly approximate the pressure gradient term in nonstaggered grids. The third numerical difficulty, which has been less addressed, is the time integrator applied to approximate the temporal derivative terms shown in the equations of motion for an incompressible fluid flow. As a fluid viscosity approaches zero, the equations of motion subject to the divergence-free constraint condition for the flow velocity vector fall into the Hamiltonian class of equations [1]. A legitimate time integrator, as a result, must be adopted for getting a proper approximation of the time derivative terms. Otherwise, both of the Hamiltonian and Casimir properties embedded in the incompressible Euler equations can by no means be well retained [2].

To resolve the above three numerical difficulties while solving the momentum equations at high Reynolds numbers, we need to enforce the continuity equation in a separate step. The theory of splitting the equations to be adopted underlies the Clebsch velocity decomposition [3]. This velocity decomposition bears a similarity to the distinguished Hodge decomposition of the velocity vectors in the incompressible Navier-Stokes equations.

When performing a numerical calculation on the time-dependent partial differential equations, one has to properly determine the grid spacing Δx and the time increment Δt. These users–chosen values have been rigorously determined as usual by conducting the modified equation analysis for the accuracy reason and performing

Von Neumann (or Fourier stability) analysis for the sake of stability enhancement. To the best of the authors' knowledge, very few or none of the previous studies have attempted to develop a rigorous means so that Δt and Δx can be well paired in the entire flow field to make the advective terms be equally predicted in each local flow field. For this reason, we are motivated in this study to locally bridge Δt and Δx through the derived optimized numerical modified wavenumber $k\Delta x$, which is the function of $\omega\Delta t$, where ω denotes the angular frequency. After choosing the values of Δt and Δx, the discretized equation obtained at a locally varying Courant number can then be used to get the dispersion relation equation–preserving solution.

The rest of this article is organized as follows. In Section 2, the incompressible Navier-Stokes equations formulated in the primitive-variable form and the three-step solution algorithm are presented. Some theoretical aspects of the Euler equations useful for approximation of the pure advection equation are also outlined. Numerical methods described in Sections 3 and 4 are developed for the approximation of the respective temporal and spatial derivative terms. The goal of approximating these derivative terms is to get better solution accuracy and at the same time to enhance numerical stability. Section 5 is devoted to the analysis of the proposed scheme. In Section 6, several benchmark problems are solved to justify the proposed discretization scheme and the applied splitting solution algorithm. The ability to get the long-term accurate solution is addressed in the result section. Some concluding remarks will be drawn in Section 7.

2. GOVERNING EQUATIONS AND SOLUTION ALGORITHM

The primitive-variable Navier-Stokes equations for modeling flow motion of an incompressible viscous fluid take the following form:

$$\frac{\partial \underline{u}}{\partial t} + (\underline{u} \cdot \nabla)\underline{u} = -\nabla p + \frac{1}{\text{Re}} \nabla^2 \underline{u} \tag{1}$$

$$\nabla \cdot \underline{u} = 0 \tag{2}$$

The above set of elliptic-parabolic differential equations derived for the primitive variables $(\underline{u}, p)$ (velocity vector, pressure) will be solved at a high Reynolds number Re. As fluid viscosity becomes zero, the resulting system of inviscid equations consists of the continuity Eq. (2) and the following incompressible Euler vector equation:

$$\frac{\partial \underline{u}}{\partial t} + (\underline{u} \cdot \nabla)\underline{u} = -\nabla p \tag{3}$$

The velocity vector shown in Eqs. (2)–(3) can be theoretically expressed in terms of the Clebsch variables λ^i and μ^i ($i = 1, 2$), thereby yielding the decomposed velocity field $\underline{u}(\underline{x}, t) = -\nabla\phi + \sum_{i=1}^{2} \lambda^i \nabla \mu^i$ [3]. These Clebsch variables are the Lagrangian invariants which remain unchanged along the fluid trajectory. In other words, Clebsch variables can be regarded as the markers of vortex lines. The scalar function $\phi(\underline{x}, t)$ shown in the above velocity decomposition equation is determined by $\nabla \cdot \underline{u} = 0$. The velocity vector is therefore the sum of the divergence-free part and the gradient part of a scalar potential [4]. Based on the theory of Clebsch

velocity decomposition [5], calculation of Eqs. (1)–(2) can be split to the respective equations for the two velocity components.

Following the above rigorous velocity decomposition [5], Eqs. (1)–(2) will be solved from the following three-step solution algorithm. To linearize the differential Eqs. in (3), in the convection step the value of $\underline{u}(\underline{x}, t = n\Delta t)$ is specified as $\underline{\bar{u}}$. The following vector equation for $\underline{u}^*$ is then solved in ω with the velocity vector $\underline{u}^*|_{t=t^n} = \underline{u}^n$ being prescribed along the boundary $\Gamma(\equiv \partial\omega)$:

$$\frac{\partial \underline{u}^*}{\partial t} + \underline{\bar{u}} \cdot \nabla \underline{u}^* = 0 \tag{4}$$

It is worth noting here that the time integrator for Eq. (4) should be symplectic. Otherwise, the well-known conserved quantities detailed in the next section cannot be numerically retained. In the diffusion step, the following parabolic equation with $\underline{u}^{**}|_{t=t^n} = \underline{u}^*|_{t=t^{n+1}}$ is solved:

$$\frac{\partial \underline{u}^{**}}{\partial t} = \frac{1}{\text{Re}} \nabla^2 \underline{u}^{**} \tag{5}$$

The velocity vector can then be further updated in the final projection step by taking the pressure gradient term into account:

$$\frac{\partial \underline{u}^{***}}{\partial t} = -\nabla p^n \tag{6}$$

where $\underline{u}^{***}|_{t=t^n} = \underline{u}^{**}|_{t=t^{n+1}}$. This updated vector $\underline{u}$ can be calculated from $\underline{u}^{n+1} = \underline{u}^{***} - \Delta t \nabla p'$. Readers can refer to [1] for additional details about the equation derived for the pressure-correction term p' and the currently employed projection solution algorithm.

3. SYMPLECTICITY-PRESERVING TEMPORAL SCHEME FOR THE EULER EQUATIONS

The two-dimensional incompressible differential system containing Eqs. (2)–(3) can be recast in terms of the vorticity $\tilde{\omega}(x, y, t)(\equiv \nabla \times \underline{u}) = -\nabla^2\psi$. Note that the streamfunction ψ is used to replace the continuity Eq. (1) by $u = \partial\psi/\partial y$ and $v = -\partial\psi/\partial x$. Because of the elimination of divergence-free Eq. (2), the quality of simulating the inviscid flow equations depends entirely on the following equation for the scalar vorticity $\tilde{\omega}$:

$$\frac{D\tilde{\omega}}{Dt} = \tilde{\omega}_t + \underline{u} \cdot \nabla\tilde{\omega} = 0 \tag{7}$$

The above equation can be also expressed as $\tilde{\omega}_t = -[\psi, \tilde{\omega}]$, where the operator $[f, g]$ performed on the scalar functions f and g is defined as $f_x g_y - f_y g_x$ [6]. Equation (7) can be also expressed as the symplectic form given by $\tilde{\omega}_t = J(\delta H/\delta\tilde{\omega})$ [7]. Note that $\delta H/\delta\tilde{\omega}$, where $\delta H = H(\tilde{\omega} + \delta\tilde{\omega}) - H(\tilde{\omega})$, is denoted as the functional or the variational derivative of the Hamiltonian functional H. The skew-symmetric

matrix J is equal to $-\partial(\tilde{\omega}, \bullet)\left[\equiv (\tilde{\omega}_x \bullet_y - \tilde{\omega}_y \bullet_x)\right]$. The Hamiltonian functional is $H(\tilde{\omega}) = -\frac{1}{2}\int_D \psi\,\tilde{\omega}\ dx\ dy$[7].

Because of the symplectic nature in the inviscid inviscid Euler equations, this distinguished geometric structure must be taken into consideration to preserve its inherent invariants [7]. The Euler equations cast in symplectic form have at least three different invariants [7]. The first integral invariant is associated with the Hamiltonian functional itself and is represented as $\delta H/\delta t = 0$. Another embedded invariant, which is normally referred to as the momentum (or impulse) invariant, involves the zero inner product of $\delta H/\delta\tilde{\omega}$ and $\tilde{\omega}_t$, or $(\delta H/\delta\omega,\ \tilde{\omega}_t) = 0$. The last invariant involves the so-called Casimir functional $\tilde{\varepsilon}(\tilde{\omega})$, which is defined by $J(\delta\tilde{\varepsilon}/\delta\tilde{\omega}) = 0$. In the hydrodynamic context, the Casimir invariants include, for example, helicity and entropy. The first and third invariants mentioned above will be chosen to justify the proper approximation of the pure advection equation.

It is now clear that the key to solving the Navier-Stokes equations turns out to be the development of a numerical method to approximate the inviscid Burgers' equation. Simulation of the nonlinear equation needs to linearize the equation first. The following linearized equation for the field variable ϕ is considered in a given flow field $\underline{u} = (u, v)$:

$$\phi_t + \underline{u} \cdot \nabla\phi = 0 \tag{8}$$

We will take the one-dimensional equation $u_t + u\,u_x = 0$ as an example to illustrate some of its intriguing mathematical properties. This model equation can be rewritten in terms of the Poisson bracket $\{u, H_1\}$ as $u_t = \{u, H_1\}$. The Poisson bracket for the two arbitrary variables F and G is defined in [2] as $\{F, G\} = -\frac{1}{3}\int_D u\left(\frac{\delta F}{\delta u}\frac{\partial}{\partial x}\frac{\delta G}{\delta u} - \frac{\delta G}{\delta u}\frac{\partial}{\partial x}\frac{\delta F}{\delta u}\right)\ dx$. The Poisson bracket $\{F, H_1\}$ turns out to be uu_x. The Hamiltonian H_1 denotes the kinetic-energy functional given by

$$H_1 = \frac{1}{2}\int_D u^2\ dx \tag{9}$$

The inviscid Burgers' equation can be also expressed as $u_t = \{u, H_2\}$ provided that the Hamiltonian defined below is adopted:

$$H_2 = \frac{1}{6}\int_D u^3\ dx \tag{10}$$

Under the circumstances, the noncanonical Poisson bracket is now changed to $\{F, G\} = -\int_D \frac{\delta F}{\delta u}\frac{\partial}{\partial x}\frac{\delta G}{\delta u}\ dx$ so as to get $\{u, H_2\} = u\,u_x$. The two invariants will be used in the results section as the guideline to examine how well the numerical scheme developed to solve the differential equation $u_t + uu_x = 0$ can retain its embedded conservation laws.

Since Eqs. (4) and (5) play the key role of solving the incompressible Navier-Stokes equations using the proposed three-step solution algorithm in Section 2, a proper approximation of the temporal and spatial derivative terms will be developed in this section. The symplecticity-preserving temporal scheme applied

to solve the pure advection equation will be developed. Other rigorous means will be also adopted in this study to approximate the spatial derivative terms in Section 4.1 so that the semidiscretized scheme has the optimized numerical dispersion relation Eq. for (8). A similar idea will be applied to solve the linear two-dimensional pure advection equation in Section 4.2. In Section 4.3, the sixth-order-accurate compact difference scheme used to solve the time-dependent diffusion equation will be presented.

Our current aim of conducting a temporal approximation of the linear model equation (8) is to preserve its embedded symplectic property. The remaining spatial derivative terms in the semidiscretized equation is then approximated in such a way as to get the corresponding discrete equation having the optimized numerical dispersion relation equation for the case investigated in a constant velocity flow field $\underline{u} = (u, v)$.

The sixth-order-accurate implicit time-stepping scheme proposed in [8] has been applied in [1] to preserve the symplectic structure in Eq. (8) iteratively. Since we aim to develop a scheme having the optimized numerical dispersion relation equation, only the noniterative symplectic time integrators can be chosen to derive the explicit semidiscretized equation. To get a symplectic scheme with the best numerical dispersion relation equation for the model Eq. (8), in this study the noniterative second-order-accurate temporal scheme given below is applied at an interior point i:

$$\frac{\phi_i^{n+1} - \phi_i^n}{\Delta t} = \frac{1}{2}\left(\underline{u} \cdot \nabla\phi^{n+1} + \underline{u} \cdot \nabla\phi^n\right) \qquad (11)$$

4. TWO-DIMENSIONAL LINEAR ADVECTION SCHEME

After approximating the time derivative term in Section 3, we proceed to discretize the first-order spatial derivative terms shown in (11). The scheme with the optimized numerical dispersion relation equation will be developed first in Section 4.1 for the one-dimensional equation and then in Section 4.2 for the two-dimensional equation.

4.1. One-Dimensional Scheme with Optimized Numerical Dispersion Relation Equation

The spatial derivative term $\partial\phi/\partial x$ at an interior node i is approximated as follows in a mesh of uniform grid spacing Δx:

$$\phi_x = \frac{1}{\Delta x}\left(a_1\phi_{i-2} + a_2\phi_{i-1} + a_3\phi_i + a_4\phi_{i+1} + a_5\phi_{i+2}\right) \qquad (12)$$

The five introduced weighting coefficients a_1 to a_5 will be rigorously determined to yield good overall accuracy. When approximating the time-dependent wave equation (8), numerical error can affect the predicted wave amplitude and propagation speed. In any simulation, numerical dissipation error can more or less smear all frequency

modes of the solution, and the dispersion error can make the numerical phase velocity frequency-dependent. Besides the reduction of amplitude error, a proper discretization method should also accommodate a numerical dispersion relation equation that matches well with the exact dispersion relation equation. To eliminate the above two error types, the modified equation analysis will be performed together with the method of minimization of the dispersive error so as to get the best numerical dispersion relation equation for the investigated pure advection equation. To get a solution with reduced dispersion errors, one can optimize the numerical wavenumber [9–11] or minimize the error between the numerical and exact dispersion relation equations [12–16].

The terms $\phi_{i\pm1}^{n+1}$, $\phi_{i\pm2}^{n+1}$, $\phi_{i\pm1}^{n}$, and $\phi_{i\pm2}^{n}$ are expanded first in Taylor series with respect to ϕ_i^n at a node i. These expansion terms are then substituted into the following discrete equation for (11):

$$\frac{\phi_i^{n+1} - \phi_i^n}{\Delta t} = \frac{u}{2\Delta x}[(a_1\phi_{i-2}^{n+1} + a_2\phi_{i-1}^{n+1} + a_3\phi_i^{n+1} + a_4\phi_{i+1}^{n+1} + a_5\phi_{i+2}^{n+1})$$
$$+ (a_1\phi_{i-2}^n + a_2\phi_{i-1}^n + a_3\phi_i^n + a_4\phi_{i+1}^n + a_5\phi_{i+2}^n)] \tag{13}$$

After a lengthy derivation, the modified equation can be derived as follows:

$$\phi_t + u\phi_x = \left\{ \frac{u}{\Delta x}[(a_1 + a_2 + a_3 + a_4 + a_5)]\phi \right\}$$
$$+ \left\{ \phi_t + \frac{u}{2\Delta x}[\Delta t(a_1 + a_2 + a_3 + a_4 + a_5)\phi_t \right.$$
$$\left. + 2\Delta x(-2a_1 - a_2 + a_4 + 2a_5)\phi_x] \right\}$$
$$+ \left\{ \frac{\Delta t}{2}\phi_{tt} + \frac{u}{2\Delta x}\left[\frac{\Delta t^2}{2}(a_1 + a_2 + a_3 + a_4 + a_5)\phi_{tt} \right.\right.$$
$$\left.\left. + \Delta t\Delta x(-2a_1 - a_2 + a_4 + 2a_5)\phi_{xt} + \Delta x^2(4a_1 + a_2 + a_4 + 4a_5)\phi_{xx} \right] \right\}$$
$$+ \left\{ \frac{\Delta t^2}{6}\phi_{ttt} + \frac{u}{4\Delta x}\left[\frac{\Delta t^3}{3}(a_1 + a_2 + a_3 + a_4 + a_5)\phi_{ttt} \right.\right.$$
$$+ \Delta t^2\Delta x(-2a_1 - a_2 + a_4 + 2a_5)\phi_{xtt} + \Delta t\Delta x^2(4a_1 + a_2 + a_4 + 4a_5)\phi_{xxt}$$
$$\left.\left. + \frac{\Delta x^3}{3}(-8a_1 - a_2 + a_4 + 8a_5)\phi_{xxx} \right] \right\} \tag{14}$$

Both of the mixed and time derivative terms shown in the above modified equation are replaced by terms $\phi_{xt} = -u\,\phi_{xx} + A\phi_{xxx} + B\phi_{xxt} + C\phi_{ttx} + \text{H.O.T.}$, $\phi_{tt} = u^2\phi_{xx} - uA\phi_{xxx} - uB\phi_{xtx} - uC\phi_{ttx} + \text{H.O.T.}$, $\phi_{xtt} = -u^2\phi_{xxx} + \text{H.O.T.}$, $\phi_{xxt} = -u\phi_{xxx} + \text{H.O.T.}$, and $\phi_{ttt} = -u^3\,\phi_{xxx} + \text{H.O.T.}$, where H.O.T. stands for higher-order terms. In the above, $A = (u\Delta x/2)(a_4 + 4a_5 + 4a_1 + a_2)$, $B = (u\Delta t/2)(-2a_2 + a_4 + 2a_5 - a_2)$, and $C = (u\Delta t^2)/4\Delta x(a_1 + a_2 + a_3 + a_4 + a_5) + (\Delta t/2)$. The four leading discretization error terms shown in the resulting modified equation of second kind

are then eliminated to get four algebraic equations. The weighting coefficients a_1, a_2, a_4, and a_5 can therefore be expressed in terms of the coefficient a_3 shown below:

$$a_1 = \frac{1}{12} + \frac{\text{Cr}^2}{24} + \frac{1}{6}a_3 \tag{15}$$

$$a_2 = -\frac{2}{3} - \frac{\text{Cr}^2}{12} - \frac{2}{3}a_3 \tag{16}$$

$$a_4 = \frac{2}{3} + \frac{\text{Cr}^2}{12} - \frac{2}{3}a_3 \tag{17}$$

$$a_5 = -\frac{1}{12} - \frac{\text{Cr}^2}{24} + \frac{1}{6}a_3 \tag{18}$$

where $\text{Cr}(\equiv u\Delta t/\Delta x)$ denotes the Courant number. It is worth nothing here that the proposed scheme depends locally on the Courant number Cr. For a unique determination of the five introduced coefficients in the approximated equation of $\partial\phi/\partial x$ at a nodal point i, one more algebraic equation needs to be derived to get the proposed Cr-dependent pure advection scheme.

While approximating the propagation equation it is essential to reduce the cumulative numerical dispersion error. In this study the last required algebraic equation is derived by minimizing the difference between the exact and numerical dispersion relation equations for the linear inviscid equation $\phi_t + u\phi_x = 0$. Note that the dispersion relation is used to link the angular frequency ω of a wave with the wavenumber k. To derive the corresponding numerical dispersion relation equation, the plane wave cast in a form of $e^{\mathbf{i}(\omega t - kx)}$ for $\phi_t + u\,\phi_x = 0$ is needed to derive the difference between the exact and numerical dispersion relation equations. This difference is then minimized to get the final algebraic equation for the closure reason.

Derivation of the last algebraic equation for the linear equation $\phi_t + u\phi_x = 0$ involves use of the harmonic ansatz $\phi(x, t) = \phi_0 e^{\mathbf{i}(\omega t - kx)}$. The differential operator in (x, t) can be transformed to its corresponding algebraic expression in (ω, k), where ω and k denote respectively the angular frequency and wavenumber. Through the transformation performed between the (x, t) and (ω, k) planes, the exact dispersion relation (or Von Neumann stability relation) equation is derived as $\omega - uk = 0$. By substituting the discrete solutions $\phi_0 e^{\mathbf{i}[\omega t - k(x \pm \Delta x)]}$, $\phi_0\,e^{\mathbf{i}[\omega t - k(x \pm 2\Delta x)]}$, $\phi_0 e^{\mathbf{i}[\omega(t + \Delta t) - k(x \pm \Delta x)]}$, and $\phi_0\,e^{\mathbf{i}[\omega(t + \Delta t) - k(x \pm 2\Delta x)]}$, which are obtained from the plane-wave solution $\phi_0 e^{\mathbf{i}(\omega t - kx)}$, into Eq. (13), the numerical dispersion relation equation for the equation $\phi_t + u\phi_x = 0$ can be derived as

$$e^{\mathbf{i}\omega_{\text{num}}\Delta t} = \frac{1 - (\text{Cr}/2)\left(a_1 e^{2\mathbf{i}k\Delta x} + a_2 e^{\mathbf{i}k\Delta x} + a_3 + a_4 e^{-\mathbf{i}k\Delta x} + a_5 e^{-2\mathbf{i}k\Delta x}\right)}{1 + (\text{Cr}/2)\left(a_1 e^{2\mathbf{i}k\Delta x} + a_2 e^{\mathbf{i}k\Delta x} + a_3 + a_4 e^{-\mathbf{i}k\Delta x} + a_5 e^{-2\mathbf{i}k\Delta x}\right)} \tag{19}$$

Having derived the above numerical dispersion relation equation, the numerical angular frequency ω_{num} is no longer linearly proportional to the wavenumber k. This means that numerical dispersion error has been introduced and can definitely affect the predicted solution.

One can reduce the dispersion error directly, by decreasing the difference between the exact and numerical dispersion relation equations, or indirectly, by minimizing the difference between the numerical and exact phase velocity or group velocity. In this study the error function $E = (\omega_{num} - \omega_{exact})^2$ is minimized in a global sense as follows within a proper integration interval of the scaled wavenumber:

$$\int_0^{m\pi} W(\omega_{num} - \omega_{exact})^2 \, d(k\Delta x) \qquad (20)$$

The reason for introducing the weighting function W into the above equation is to make Eq. (20) numerically integrable. To avoid the so-called aliasing error, one needs further to determine the value of m in $0 \le m \le 1$.

By applying the limiting condition $\partial E/\partial a_3 = 0$, the final algebraic equation required to close the algebraic equations for a_1–a_5 is obtained. The equation derived from the above error minimization can then be used together with the other four algebraic equations in (15)–(18), which were derived on the basis of the modified equation analysis of second kind, to uniquely determine all the five introduced parameters. The resulting derived coefficients will not be explicitly shown in this article because they are complex functions of m and $\text{Cr}(\equiv u\Delta t/\Delta x)$. The dimensionless frequency errors $(\omega_{num} - \omega_{exact})/\omega_{exact}$ derived at different Courant numbers are plotted versus the wavenumber k in Figure 1. Based on our detailed analysis, the coefficients a_1–a_5 computed at $m = \frac{6}{7}\pi$ are tabulated in Table 1. The leading discretization errors τ_4 for the term ϕ_{xxxx} in the derived modified equation are plotted with respect to Cr in Figure 2 for $m = \frac{6}{7}\pi$.

It is worth noting here that the values of the five weighting coefficients shown in (12) are not fixed throughout the domain. These values vary locally according to
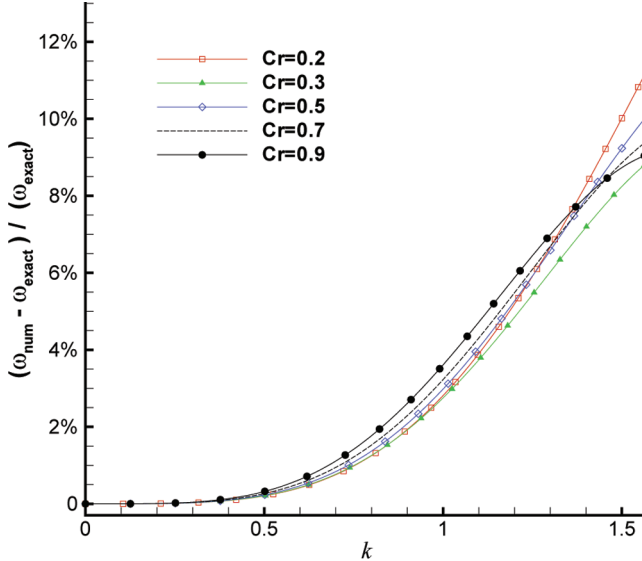

Figure 1. Dimensionless errors of the derived numerical angular frequency $(\omega_{num} - \omega_{exact})/\omega_{exact}$ plotted with respect to wavenumber k at $\text{Cr} = 0.2$, 0.3, 0.5, 0.7, and 0.9 (color figure available online).

Table 1. Weighting coefficients a_1–a_5 derived at different Courant numbers Cr

Crai	a_1	a_2	a_3	a_4	a_5
0.1	0.69231	−3.10174	3.65137	−1.76674	0.52481
0.2	0.61889	−2.80555	3.20333	−1.46555	0.44889
0.3	0.54630	−2.51103	2.75529	−1.16269	0.37213
0.4	0.43572	−2.06287	2.07431	−0.70287	0.25572
0.5	0.37833	−1.82583	1.70750	−0.45083	0.19083
0.6	0.35188	−1.71085	1.52127	−0.31751	0.15521
0.7	0.34388	−1.66801	1.44077	−0.25301	0.13638
0.8	0.34770	−1.67079	1.42618	−0.23079	0.12770
0.9	0.36041	−1.70749	1.45998	−0.23915	0.12625
1.0	0.37396	−1.74585	1.49378	−0.24585	0.12396

the flow velocity. Given the user's prescribed Δt and Δx, the local Courant number Cr is determined from the value of u. Based on the locally varying values of Cr, the corresponding weighting coefficients can be obtained by interpolating the weighting coefficients tabulated in Table 1. Use of the resulting determined locally varying weighting coefficients enables us to get a solution that can theoretically optimize the numerical dispersion relation equation at each grid point.

4.2. Two-Dimensional Scheme with Optimized Numerical Dispersion Relation Equation

In the development of the current two-dimensional pure advection scheme at a positive velocity condition (or $u > 0$ and $v > 0$), the derivative terms $(\partial \phi / \partial x)|_{i,j}$ and
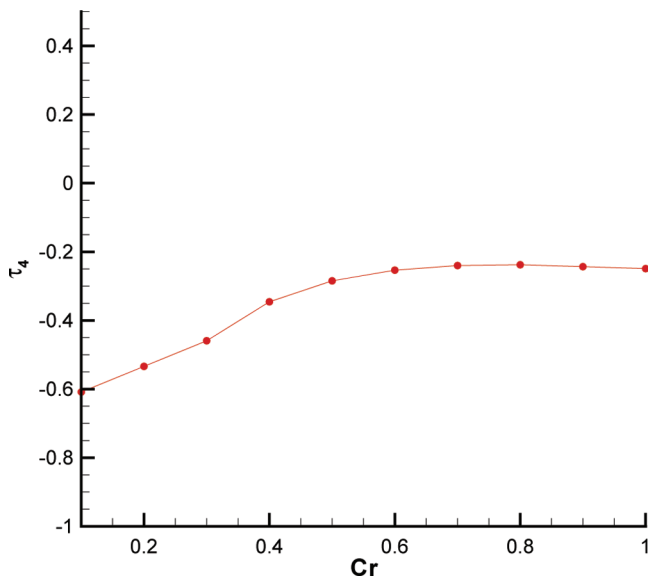

Figure 2. Coefficients of the leading discretization error shown in the derived modified equation of second kind plotted with respect to Courant numbers Cr at $m = \frac{6}{7}\pi$ (color figure available online).

$(\partial\phi/\partial y)|_{i,j}$ are approximated as follows using the nodal values of $\phi_{i,\,j}$, $\phi_{i\pm1,\,j}$, $\phi_{i,\,j\pm1}$, $\phi_{i\pm2,\,j}$, $\phi_{i,\,j\pm2}$:

$$\frac{\partial\phi}{\partial x}\bigg|i,j = \frac{1}{\Delta x}\left(a_1\phi_{i-2,j} + a_2\phi_{i-1,j} + a_3\phi_{i,j} + a_4\phi_{i+1,j} + a_5\phi_{i+2,j}\right) \tag{21}$$

$$\frac{\partial\phi}{\partial y}\bigg|i,j = \frac{1}{\Delta y}\left(a_1\phi_{i,j-2} + a_2\phi_{i,j-1} + a_3\phi_{i,j} + a_4\phi_{i,j+1} + a_5\phi_{i,j+2}\right) \tag{22}$$

The wave solution $e^{\mathbf{i}(\omega t - k_x x - k_y y)}$ is substituted first into (21)–(22). The resulting equations are then plugged into the proposed midpoint time-stepping equation $\frac{\phi_{i,j}^{n+1}-\phi_{i,j}^{n}}{\Delta t} + \frac{u}{2}(\phi_x^{n+1} + \phi_x^{n}) + \frac{v}{2}(\phi_y^{n+1} + \phi_y^{n}) = 0$. The numerical dispersion relation equation is derived as follows after a lengthy algebraic derivation:

$$e^{\mathbf{i}\omega_{\text{num}}\Delta t} = \frac{1 - \alpha_1 - \alpha_2}{1 + \alpha_1 + \alpha_2} \tag{23}$$

In the above, α_1 and α_2 are expressed as

$$\alpha_1 = \frac{\text{Cr}_x}{2}\left(a_1 e^{2\mathbf{i}k_x\Delta x} + a_2 e^{\mathbf{i}k_x\Delta x} + a_3 + a_4 e^{-\mathbf{i}k_x\Delta x} + a_5 e^{-2\mathbf{i}k_x\Delta x}\right) \tag{24}$$

$$\alpha_2 = \frac{\text{Cr}_y}{2}\left(a_1 e^{2\mathbf{i}k_y\Delta y} + a_2 e^{\mathbf{i}k_y\Delta y} + a_3 + a_4 e^{-\mathbf{i}k_y\Delta y} + a_5 e^{-2\mathbf{i}k_y\Delta y}\right) \tag{25}$$

For the rest of the flow directions, one can similarly derive their corresponding numerical dispersion equations with the expressions of α_1 and α_2 summarized in Table 2.

Following the same method of minimization of error described in Section 4.1 for the one-dimensional equation, the weighting coefficients and the integration

Table 2. Expressions of α_1 and α_2 shown in the numerical dispersion relation equation $e^{\mathbf{i}\omega_{\text{num}}\Delta t} = (1 - \alpha_1 - \alpha_2)/(1 + \alpha_1 + \alpha_2)$ are summarized for all the four possible velocity directions

	α_1 and α_2
$u>0$, $v>0$	$\alpha_1 = \frac{\text{Cr}_x}{2}\left(a_1 e^{2\mathbf{i}k_x\Delta x} + a_2 e^{\mathbf{i}k_x\Delta x} + a_3 + a_4 e^{-\mathbf{i}k_x\Delta x} + a_5 e^{-2\mathbf{i}k_x\Delta x}\right)$
	$\alpha_2 = \frac{\text{Cr}_y}{2}\left(a_1 e^{2\mathbf{i}k_y\Delta y} + a_2 e^{\mathbf{i}k_y\Delta y} + a_3 + a_4 e^{-\mathbf{i}k_y\Delta y} + a_5 e^{-2\mathbf{i}k_y\Delta y}\right)$
$u<0$, $v>0$	$\alpha_1 = -\frac{\text{Cr}_x}{2}\left(a_5 e^{2\mathbf{i}k_x\Delta x} + a_4 e^{\mathbf{i}k_x\Delta x} + a_3 + a_2 e^{-\mathbf{i}k_x\Delta x} + a_1 e^{-2\mathbf{i}k_x\Delta x}\right)$
	$\alpha_2 = \frac{\text{Cr}_y}{2}\left(a_1 e^{2\mathbf{i}k_y\Delta y} + a_2 e^{\mathbf{i}k_y\Delta y} + a_3 + a_4 e^{-\mathbf{i}k_y\Delta y} + a_5 e^{-2\mathbf{i}k_y\Delta y}\right)$
$u<0$, $v<0$	$\alpha_1 = -\frac{\text{Cr}_x}{2}\left(a_5 e^{2\mathbf{i}k_x\Delta x} + a_4 e^{\mathbf{i}k_x\Delta x} + a_3 + a_2 e^{-\mathbf{i}k_x\Delta x} + a_1 e^{-2\mathbf{i}k_x\Delta x}\right)$
	$\alpha_2 = -\frac{\text{Cr}_y}{2}\left(a_5 e^{2\mathbf{i}k_y\Delta y} + a_4 e^{\mathbf{i}k_y\Delta y} + a_3 + a_2 e^{-\mathbf{i}k_y\Delta y} + a_1 e^{-2\mathbf{i}k_y\Delta y}\right)$
$u>0$, $v<0$	$\alpha_1 = \frac{\text{Cr}_x}{2}\left(a_1 e^{2\mathbf{i}k_x\Delta x} + a_2 e^{\mathbf{i}k_x\Delta x} + a_3 + a_4 e^{-\mathbf{i}k_x\Delta x} + a_5 e^{-2\mathbf{i}k_x\Delta x}\right)$
	$\alpha_2 = -\frac{\text{Cr}_y}{2}\left(a_5 e^{2\mathbf{i}k_y\Delta y} + a_4 e^{\mathbf{i}k_y\Delta y} + a_3 + a_2 e^{-\mathbf{i}k_y\Delta y} + a_1 e^{-2\mathbf{i}k_y\Delta y}\right)$

Table 3. Weighting coefficients a_3 computed at different Courant numbers Cr, tabulated for the cases $u > 0$, $v > 0$, and $u < 0$, $v < 0$

$\text{Cr}_y \backslash \text{Cr}_x$	$\text{Cr}_x = 0.1$	$\text{Cr}_x = 0.2$	$\text{Cr}_x = 0.3$	$\text{Cr}_x = 0.4$	$\text{Cr}_x = 0.5$
$\text{Cr}_y = 0.1$	5.44105	2.99033	2.24791	1.83081	1.60671
$\text{Cr}_y = 0.2$	2.99643	2.26889	1.87781	1.65985	1.54866
$\text{Cr}_y = 0.3$	2.26358	1.88675	1.68030	1.57718	1.53822
$\text{Cr}_y = 0.4$	1.85637	1.67707	1.58507	1.55392	1.56545
$\text{Cr}_y = 0.5$	1.63895	1.57132	1.55159	1.57132	1.62451
$\text{Cr}_y = 0.6$	1.53440	1.53150	1.56098	1.62206	1.66661
$\text{Cr}_y = 0.7$	1.49961	1.53904	1.60779	1.68495	1.70871
$\text{Cr}_y = 0.8$	1.51584	1.59099	1.67427	1.69886	1.68107
$\text{Cr}_y = 0.9$	1.58411	1.66716	1.68807	1.66945	1.63733
$\text{Cr}_y = 1.0$	1.65445	1.67191	1.65488	1.62397	1.58853

$\text{Cr}_y \backslash \text{Cr}_x$	$\text{Cr}_x = 0.6$	$\text{Cr}_x = 0.7$	$\text{Cr}_x = 0.8$	$\text{Cr}_x = 0.9$	$\text{Cr}_x = 1.0$
$\text{Cr}_y = 0.1$	1.49943	1.46474	1.48068	1.54251	1.64569
$\text{Cr}_y = 0.2$	1.50638	1.51283	1.56179	1.65120	1.70935
$\text{Cr}_y = 0.3$	1.54420	1.58848	1.66436	1.71424	1.70837
$\text{Cr}_y = 0.4$	1.61211	1.68042	1.71676	1.70769	1.67864
$\text{Cr}_y = 0.5$	1.69144	1.71803	1.70422	1.67400	1.63807
$\text{Cr}_y = 0.6$	1.71564	1.69885	1.66727	1.63098	1.54832
$\text{Cr}_y = 0.7$	1.69108	1.65889	1.62232	1.58502	1.54832
$\text{Cr}_y = 0.8$	1.64885	1.61233	1.57518	1.53876	1.50349
$\text{Cr}_y = 0.9$	1.60110	1.56427	1.52822	1.49338	1.45981
$\text{Cr}_y = 1.0$	1.55230	1.51676	1.48243	1.44941	1.41756

parameter m are determined from the modified equation of second kind and the minimization analysis. For completeness, in Table 3 and Table 4 the values of a_3 are tabulated with respect to $\text{Cr}_x (\equiv u\Delta x / \Delta t)$ and $\text{Cr}_y (\equiv v\Delta y / \Delta t)$ at $m = \frac{6}{7}\pi$. Note that this value of m has been numerically shown to yield the smallest aliasing error. Having obtained these Courant number–dependent weighting coefficients a_3, the rest of the four weighting coefficients can then be determined accordingly.

The five weighting coefficients, which can lead to the optimized numerical dispersion relation equation, are also plotted versus the flow angle $\tan^{-1}(u/v)$ in Figure 3. Like the one-dimensional scheme, through the interpolation means the two-dimensional numerical dispersion relation equation–preserving solution can be obtained according to the local fluid velocities $u(x, y)$, $v(x, y)$, and the user's chosen values of Δt, Δx, and Δy.

4.3. Sixth-Order-Accurate Compact Difference Scheme for the Diffusion Equation

The parabolic equation (5) will be discretized first using the Euler time-stepping scheme for $\partial u / \partial t$ to yield the differential equation $\nabla^2 \underline{u}|^{n+1} - \frac{\text{Re}}{\Delta t}\underline{u}|^{n+1} = -\frac{\text{Re}}{\Delta t}\underline{u}|^n$. The approximation error for $\partial^2 u / \partial x^2$ is normally dissipative. For this reason, the following centered compact finite-difference scheme for $\partial^2 u / \partial x^2$ at an interior node i, for example, is applied:

Table 4. Weighting coefficients a_3 computed at different Courant numbers Cr, tabulated for the cases $u > 0$, $v < 0$, and $u < 0$, $v > 0$

$Cr_y \backslash Cr_x$	$Cr_x = 0.1$	$Cr_x = 0.2$	$Cr_x = 0.3$	$Cr_x = 0.4$	$Cr_x = 0.5$
$Cr_y = 0.1$	5.69838	4.29855	2.88573	2.21231	1.87091
$Cr_y = 0.2$	4.30395	4.21349	2.91066	2.34872	2.04423
$Cr_y = 0.3$	2.90162	3.00799	2.93559	2.52462	2.25417
$Cr_y = 0.4$	2.23938	2.36922	2.53643	2.55821	2.46715
$Cr_y = 0.5$	1.90521	2.07046	2.27307	2.47643	2.59123
$Cr_y = 0.6$	1.74118	1.93444	2.17130	2.48032	2.76847
$Cr_y = 0.7$	1.71046	1.89928	2.21035	2.55138	2.73854
$Cr_y = 0.8$	1.67975	1.95990	2.25224	2.42555	2.55757
$Cr_y = 0.9$	1.73708	2.00228	2.15726	2.27670	2.38273
$Cr_y = 1.0$	1.79442	1.93602	2.06227	2.13982	2.22888

$Cr_y \backslash Cr_x$	$Cr_x = 0.6$	$Cr_x = 0.7$	$Cr_x = 0.8$	$Cr_x = 0.9$	$Cr_x = 1.0$
$Cr_y = 0.1$	1.70376	1.56146	1.63921	1.70340	1.80612
$Cr_y = 0.2$	1.92546	1.86669	1.91375	2.01469	2.00153
$Cr_y = 0.3$	2.14717	2.17191	2.26738	2.21578	2.12726
$Cr_y = 0.4$	2.45452	2.55966	2.46989	2.34323	2.22508
$Cr_y = 0.5$	2.76188	2.76054	2.60094	2.44064	2.30943
$Cr_y = 0.6$	3.01748	2.91217	2.71411	2.53747	2.38734
$Cr_y = 0.7$	2.89699	2.96474	2.81803	2.62813	2.46378
$Cr_y = 0.8$	2.68027	2.79883	2.82821	2.70428	2.53941
$Cr_y = 0.9$	2.48484	2.58937	2.68319	2.69643	2.59489
$Cr_y = 1.0$	2.31640	2.46703	2.53817	2.57276	2.57753

$$\bar{b}_1 \frac{\partial^2 u}{\partial x^2}\bigg|_{i-1} + \frac{\partial^2 u}{\partial x^2}\bigg|_i + \bar{b}_3 \frac{\partial^2 u}{\partial x^2}\bigg|_{i+1} = \frac{1}{h^2}(\bar{c}_1 u_{i-1} + \bar{c}_2 u_i + \bar{c}_3 u_{i+1})$$

$$-\frac{1}{h}\left(\bar{a}_1 \frac{\partial u}{\partial x}\bigg|_{i-1} + \bar{a}_2 \frac{\partial u}{\partial x}\bigg|_{i+\bar{a}_3} \frac{\partial u}{\partial x}\bigg|_{i+1}\right) \tag{26}$$

The weighing coefficients in (26) can be determined solely from the classical modified equation analysis for the sake of getting better accuracy. Along the line of this thought, all the coefficients shown above are derived as $\bar{a}_1 = -\frac{9}{8}, \bar{a}_2 = 0, \bar{a}_3 = \frac{9}{8}, \bar{b}_1 = -\frac{1}{8}, \bar{c}_1 = 3, \bar{c}_2 = -6$, and $\bar{c}_3 = 3$. Use of this set of the derived coefficients yields the sixth-order-accurate modified equation for $\partial^2 u/\partial x^2$ [17].

5. SOME NUMERICAL INSIGHTS IN THE PROPOSED SCHEME

The numerical angular frequency ω_{num} and the numerical group velocity $d\omega_{num}/dk$ are derived first. They are then plotted with respect to the wavenumber k in Figure 4 and Figure 5, respectively, at different Courant numbers using the currently proposed method. For completeness, Fourier (or von Neumann) stability analysis [18] is also conducted to get the following amplification factor $G(\equiv \phi_i^{n+1}/\phi_i^n)$, which is the function of $\beta = k\Delta x$ and $Cr = u\Delta t/\Delta x$:
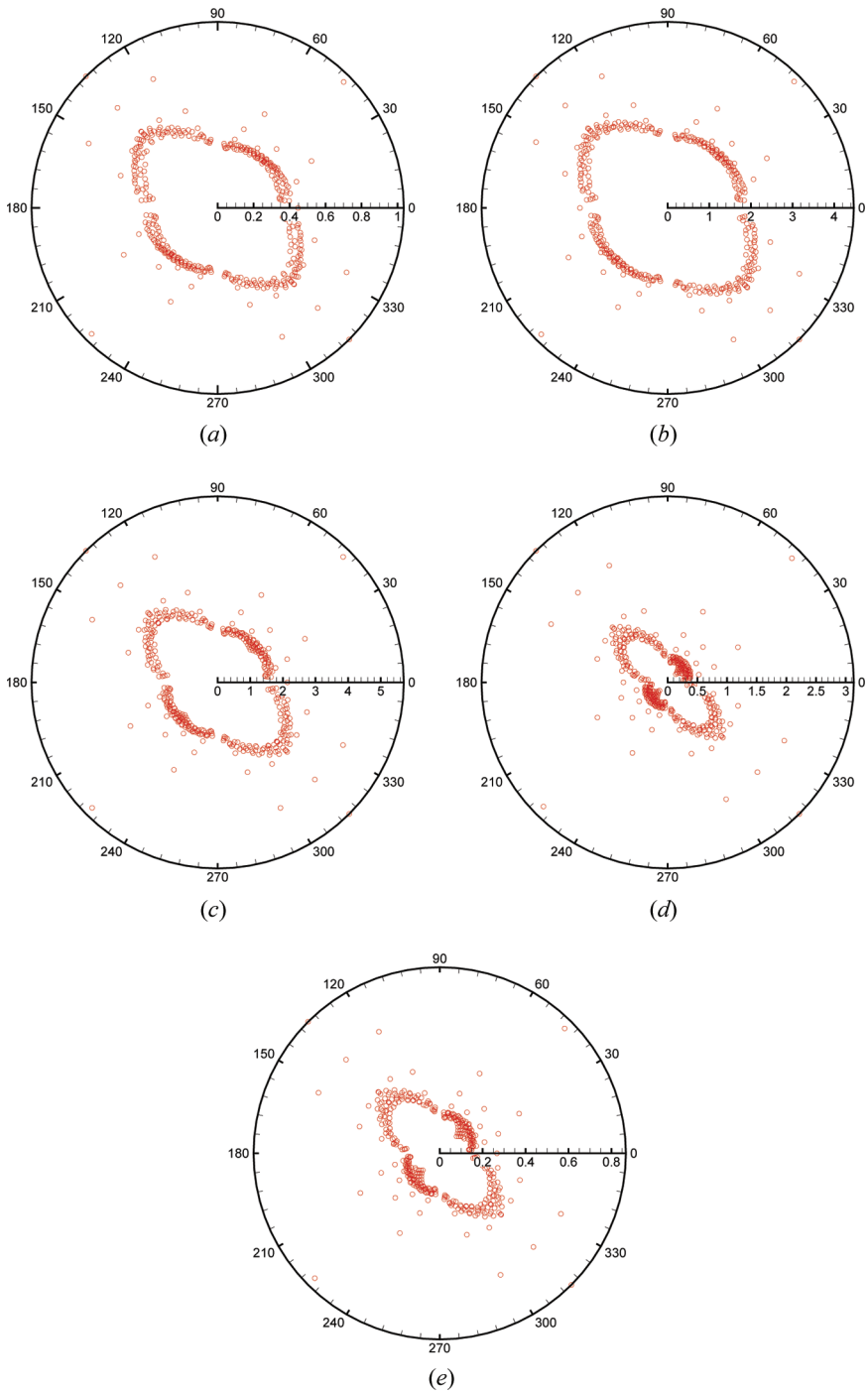
Figure 3. The five derived weighting coefficients are plotted with respect to flow angle $\tan^{-1}(u/v)$ ranging between $0°$ and $360°$: (*a*) a_1; (*b*) a_2; (*c*) a_3; (*d*) a_4; (*e*) a_5 (color figure available online).
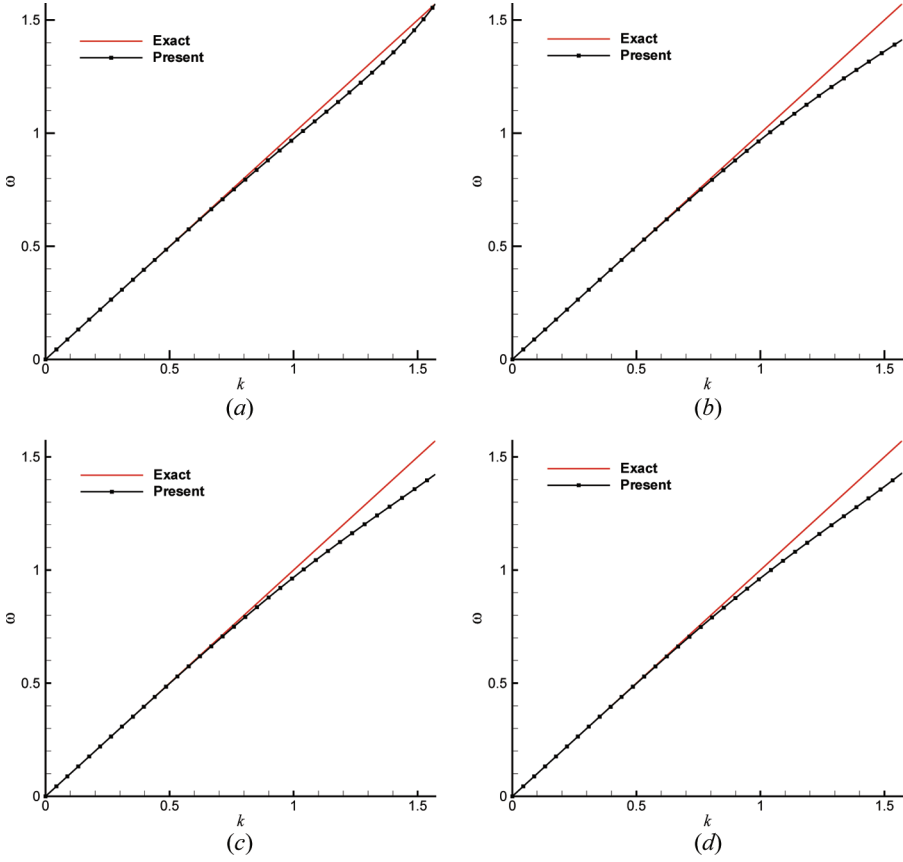
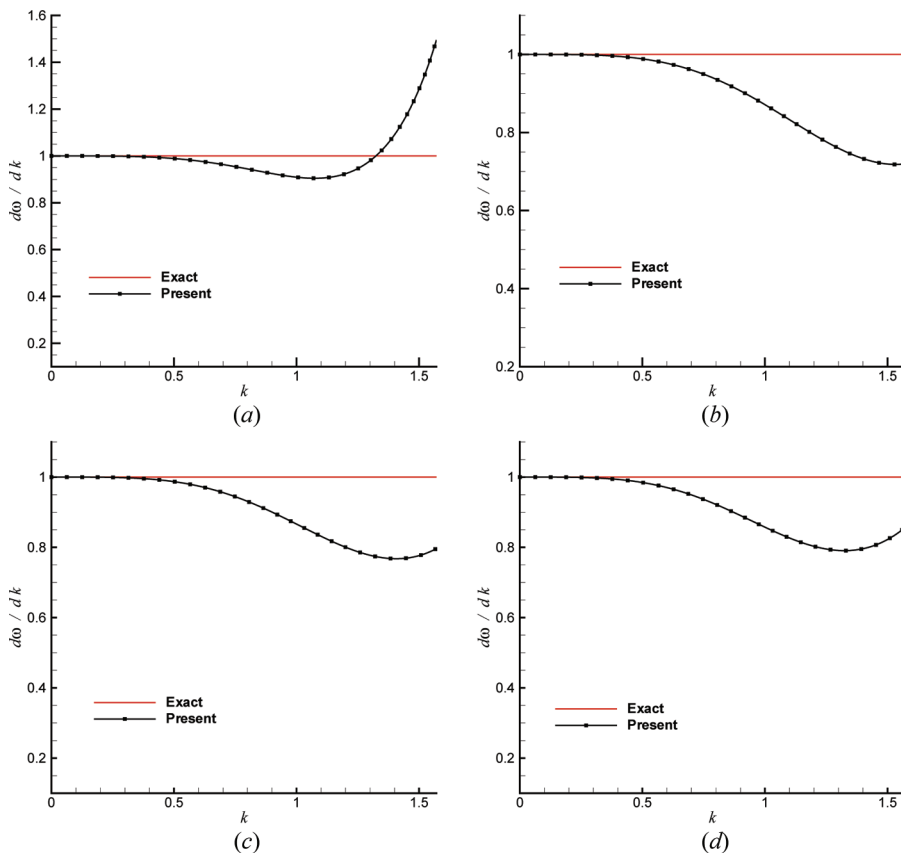**Figure 4.** Comparison of the numerical angular frequencies ω, which are plotted with respect to wavenumber k, at four different values of $\mathrm{Cr}(\equiv u\Delta t/\Delta x)$: (a) 0.3; (b) 0.5; (c) 0.7; (d) 0.9 (color figure available online).

$$G = \frac{1 - (\mathrm{Cr}/2)(a_1 e^{-2\beta\mathbf{i}} + a_2 e^{-\beta\mathbf{i}} + a_3 + a_4 e^{\beta\mathbf{i}} + a_5 e^{2\beta\mathbf{i}})}{1 + (\mathrm{Cr}/2)(a_1 e^{-2\beta\mathbf{i}} + a_2 e^{-\beta\mathbf{i}} + a_3 + a_4 e^{\beta\mathbf{i}} + a_5 e^{2\beta\mathbf{i}})} \tag{27}$$

The derived amplification factor is plotted in Figure 6a at different values of the Courant number. Since the absolute values of G are all smaller than 1, the proposed scheme is unconditionally stable.

The amplification factor can be also rewritten in the following equivalent exponential form as $G = |G|e^{\mathbf{i}\theta}$, where $\theta(\equiv \tan^{-1}[\mathrm{Im}(G)/\mathrm{Re}(G)])$ is the phase angle. Given the exact phase angle θ_e, which is equal to $-\beta\,\mathrm{Cr}$, the following relative phase shift can be used in the following comparison study:

$$\frac{\theta}{\theta_e} = \frac{\tan^{-1}[\mathrm{Im}(G)/\mathrm{Re}(G)]}{-\beta\,\mathrm{Cr}} \tag{28}$$

In Figure 6b, the relative phase shift θ/θ_e is plotted at different values of the Courant number.

Figure 5. Comparison of the derived numerical group velocities $d\omega/dk$, which are plotted with respect to wavenumber k, at four different values of Cr($\equiv u\Delta t/\Delta x$): (*a*) 0.3; (*b*) 0.5; (*c*) 0.7; (*d*) 0.9 (color figure available online).

6. NUMERICAL RESULTS

The pure advection equation is solved in Section 6.1 to verify the developed symplectic advection scheme. This scheme will be also numerically shown to have a good numerical dispersion relation equation for the pure advection equation. The proposed symplecticity and dispersion relation equation–preserving scheme is then applied to solve incompressible inviscid flow equations in Section 6.2. Two unsteady Navier-Stokes problems in Section 6.3 are also investigated. Finally, a coupled system of the hydrodynamic and level-set equations for modeling the bubble rising and droplet falling problems are investigated in Section 6.4.

6.1. One-Dimensional Pure Advection Problems

The one-dimensional linear equation $\phi_t + \phi_x = 0$ is solved subject to the following initial condition [12]:
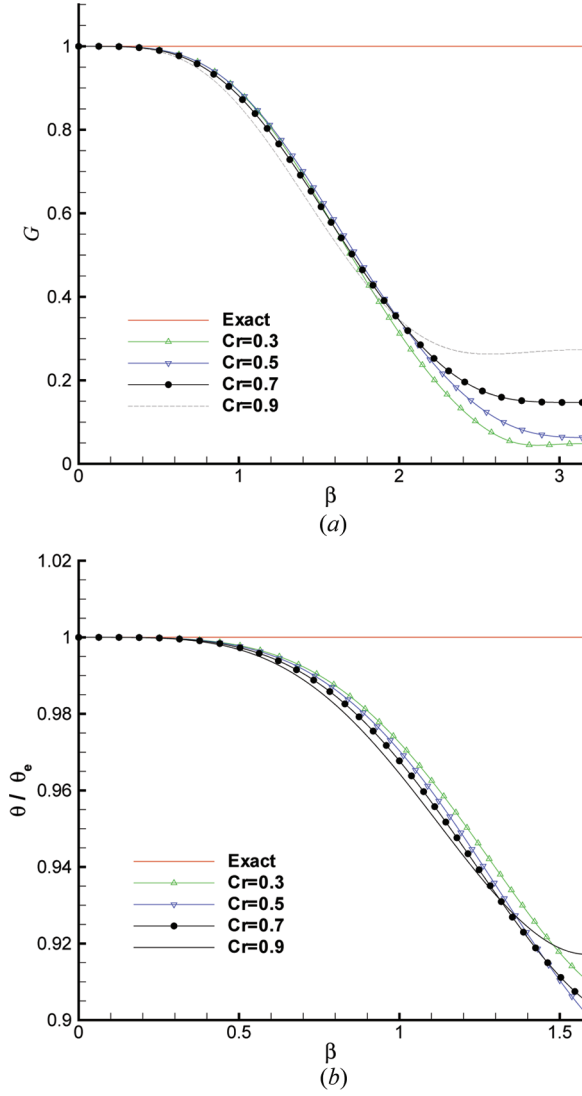
Figure 6. (*a*) Amplification factors *G* of the proposed scheme plotted with respect to β at four different values of Cr($\equiv u\Delta t/\Delta x$). (*b*) Relative ratios θ/θ_e plotted with respect to β at four different values of Cr($\equiv u\Delta t/\Delta x$) (color figure available online).

$$u(x,0) = \begin{cases} \frac{1}{6}[G(x,\tilde{\beta},z-\delta) + 4\,G(x,\tilde{\beta},z-\delta) + G(x,\tilde{\beta},z+\delta)] & -0.8 \leq x \leq -0.6 \\ 1 & -0.4 \leq x \leq -0.2 \\ 1 - 10|(x-0.1)| & 0 \leq x \leq 0.2 \\ \frac{1}{6}[F(x,\alpha,a-\delta) + 4\,F(x,\alpha,a-\delta) + F(x,\alpha,a+\delta)] & 0.4 \leq x \leq 0.6 \\ 0 & \text{otherwise} \end{cases}$$

$$(29)$$

In the above, $G(\alpha, \tilde{\beta}, z) = e^{-\tilde{\beta}(x-z)^2}$ and $F(x, \alpha, a) = \mathbf{max}[1 - \alpha^2(x-a)^2, \alpha]$, where $z = -0.7$, $\tilde{\beta} = (\mathbf{log\ 2}/36\delta^2)$, $a = 0.5$, $\alpha = 10$, and $\delta = 0.005$. In this verification study, the periodic boundary condition is imposed. The time step is chosen to be $\Delta t = 0.9\Delta x$ in all computations. Figure 7 shows the exact waveform and the waveform obtained by the present scheme at $t = 2$ without adding a flux or a slope limiter to resolve oscillations near the points of discontinuity. Since the proposed scheme is not classified as a monotone scheme, the predicted kinks near the root of the square wave are computationally inevitable.

6.2. Two-Dimensional Pure Advection Problems

6.2.1. Slotted (Zalesak's) disk problem. Zalesak's problem [19] is a well-known benchmark problem for verifying the developed advection scheme. A slotted disk with a radius of 15.0 and a slot width of 5.0 is initially located at (50.0, 75.0) in a square of length 100. The prescribed velocity field is given by $u = \pi(50 - y)/314$ and $v = \pi(x - 50)/314$. The results predicted at $\Delta t = 2.0\Delta x$ in the domain of 200×200 mesh points are plotted in Figure 8a. We also plot in Fig. 8b the solution profile $\phi(x, 75)$ at $t = 200\pi$ to show good agreement between the exact (or initial) and computed solutions.

6.2.2. Mixing of cold and warm fronts. To show that our proposed numerical method has the ability of resolving interior sharp profiles, a problem containing cold and warm fronts is considered in a square domain $-4 \le x, y \le 4$. Initially, the temperature is given by $\phi(x, y, t = 0) = -\tan h(y/2)$. Subsequent to $t = 0$, the temperature is changed with time by the given rotating velocity field that
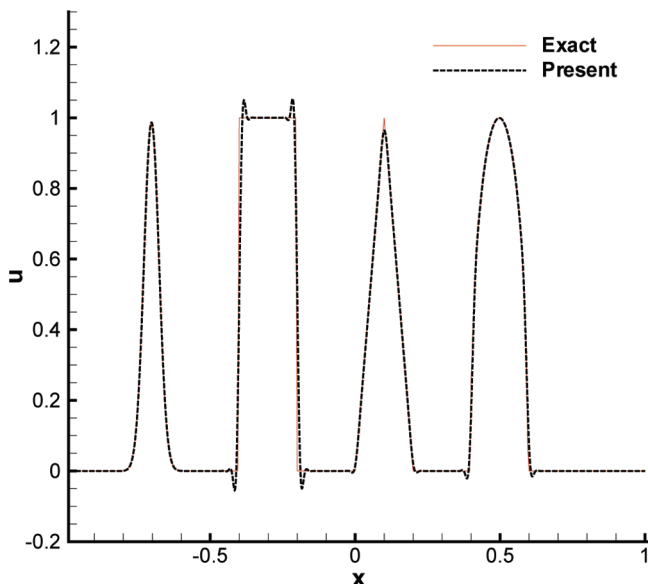
Figure 7. Comparison of the predicted and exact solutions at $t = 2$ (color figure available online).
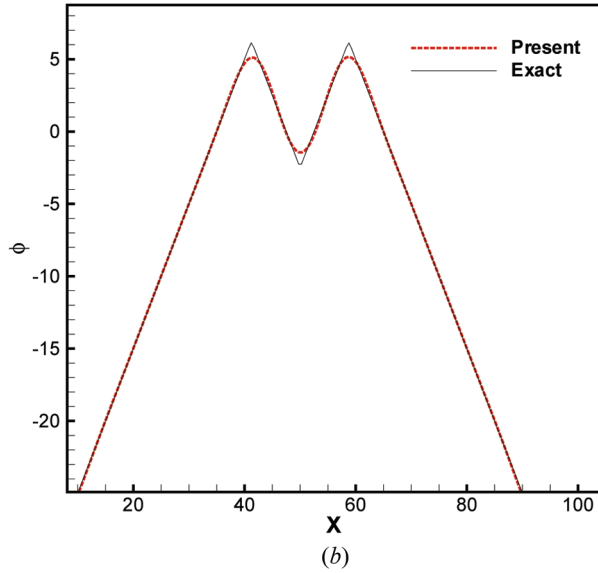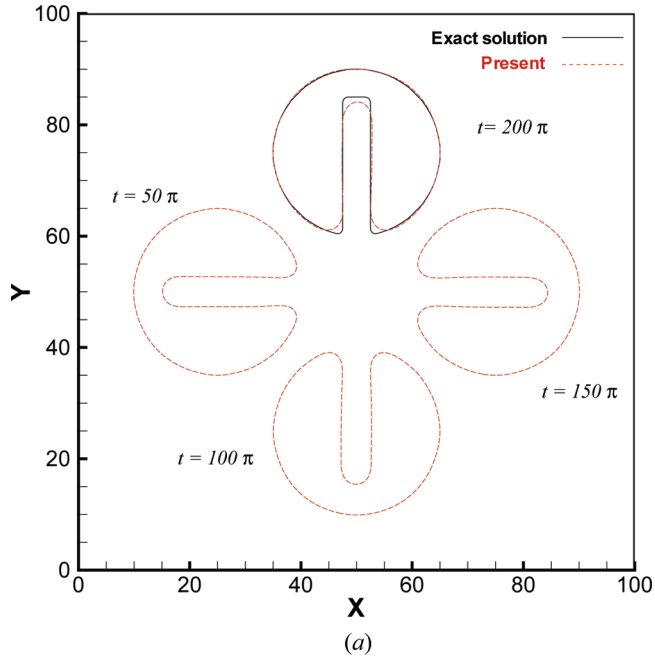
Figure 8. (*a*) Contours of $\phi = 0$ plotted at four different times. (*b*) Predicted and exact solutions for $\phi(x, 75)$ at $t = 200\pi$ (color figure available online).

is centered at the origin $(-\overline{T}y/r, \overline{T}x/r)$. Here, $\overline{T}\left(\equiv \frac{\sec^2(r)\tanh(r)}{\mathbf{max}[\sec^2(r)\tanh(r)]}\right)$ denotes the ratio of the tangential velocity at the location that is distant from $(0, 0)$ with the length of r. Due to this rotating velocity field, a marked change of the temperature can be seen
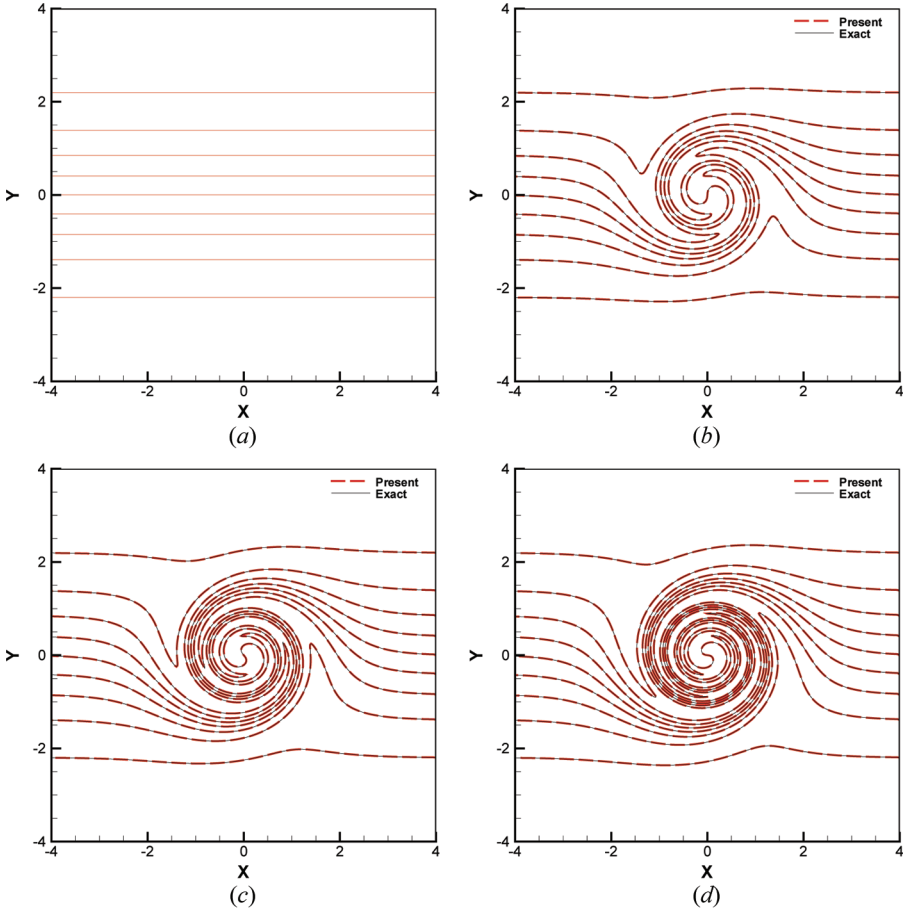
Figure 9. Predicted results plotted at four different times: (*a*) $t = 0$; (*b*) $t = 3.0$; (*c*) $t = 4.5$; (*d*) $t = 6.0$ (color figure available online).

across the interface between the warm and cold fluids. In Figure 9, one can see that the rotating flow distorts the initially sharp temperature profile. As a result, a spiral temperature profile gradually appears. For the sake of comparison, we also plot the exact solution $\phi(x, y, t)_{\text{exact}} = -\tanh\left[\frac{y}{2}\cos(\overline{\omega}t) - \frac{x}{2}\sin(\overline{\omega}t)\right]$ [20], where $\overline{\omega} = \overline{T}/r$ denotes the rotation frequency. The agreement between the simulated and exact solutions shown later in Figure 12 is excellent.

6.2.3. Twisting–untwisting problem. Given the following initial data,

$$\phi(x, t = 0) = \begin{cases} 1 & \text{if } 0 \leq x \leq 1 \text{ and } 0.4 \leq y \leq 0.6 \\ 0 & \text{otherwise} \end{cases} \tag{30}$$

the solution ϕ will be computed from the pure advection equation in the velocity field $u = \cos[\pi(x - 0.5)]\sin[\pi(y - 0.5)]$ and $v = -\sin[\pi(x - 0.5)]\cos[\pi(y - 0.5)]$ in
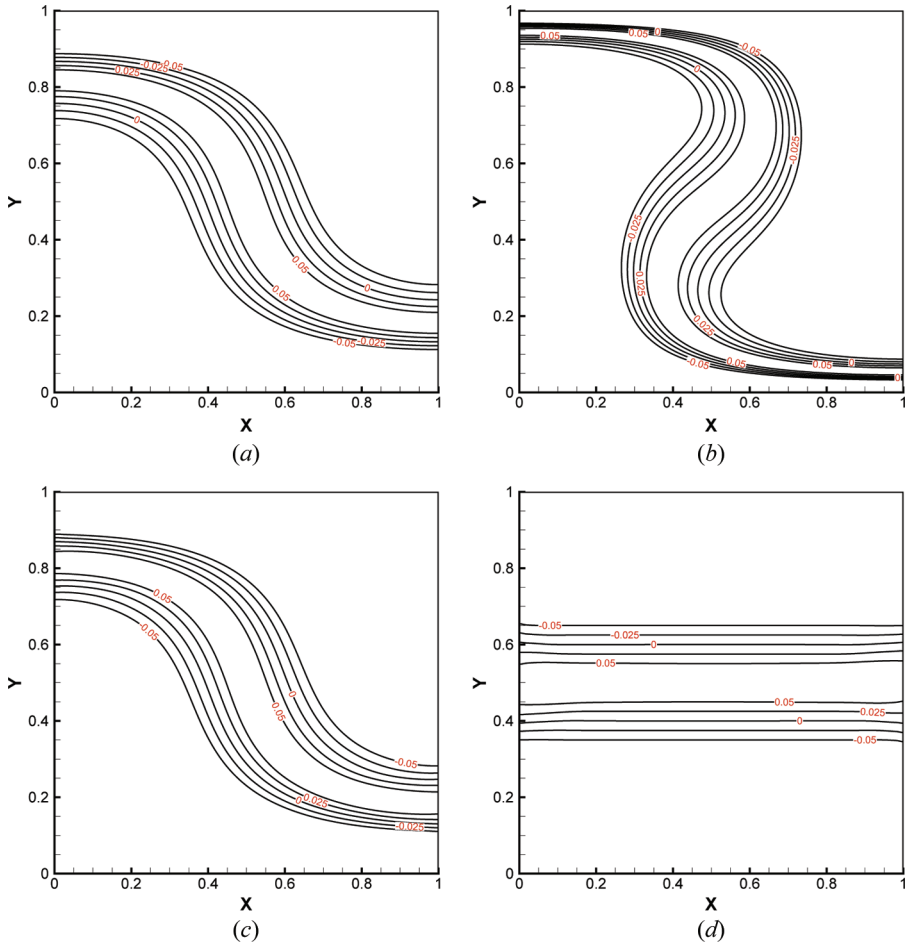
Figure 10. Predicted results plotted at four different times: (a) $t = \frac{\pi}{8}$; (b) $t = \frac{\pi}{4}$; (c) $t = \frac{3\pi}{8}$; (d) $t = \frac{\pi}{2}$ (color figure available online).

[21]. At $t = \pi/4$, the solution profile becomes exactly the same as the initial shape. For the calculations performed at $\Delta t = \pi/4\Delta x$, the solution shown in Figure 10 is computed in the mesh of 200×200 nodal points. The phase of the solution is seen to be excellently predicted, without showing any oscillation.

6.3. Incompressible Flow Problems

6.3.1. Taylor vortex problem. The problem regarding the transport of decaying Taylor vortices is frequently used as the benchmark test for the verification of numerical schemes developed to solve the unsteady fluid flow [22]. The initially periodic vortex flow is convected and decayed exponentially with time due to the nonzero fluid viscosity in the flow. The exact solution of this problem is varied with the Reynolds number Re as follows:

$$\begin{cases} u(x, y, t) = -\cos(x)\sin(y)\exp\left(\frac{-2t}{\mathrm{Re}}\right), \\ v(x, y, t) = \cos(y)\sin(x)\exp\left(\frac{-2t}{\mathrm{Re}}\right), \\ p(x, y, t) = -0.25[\cos(2x) + \cos(2y)]\exp\left(\frac{-4t}{\mathrm{Re}}\right) \end{cases} \tag{31}$$

(a)

(b)
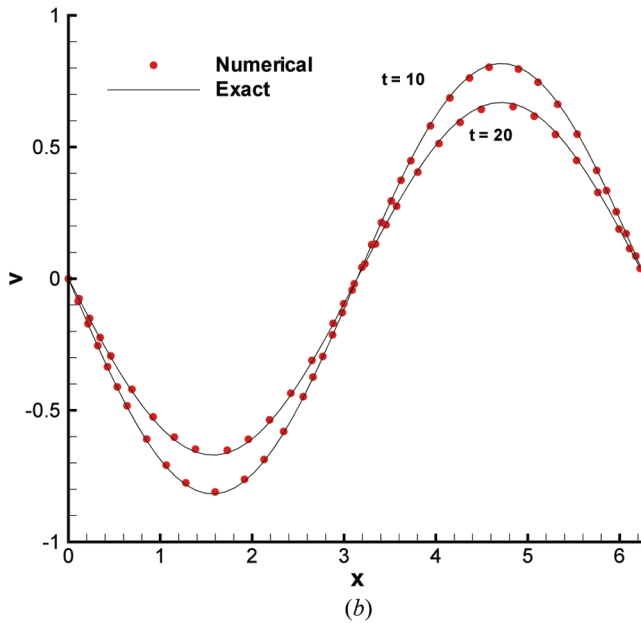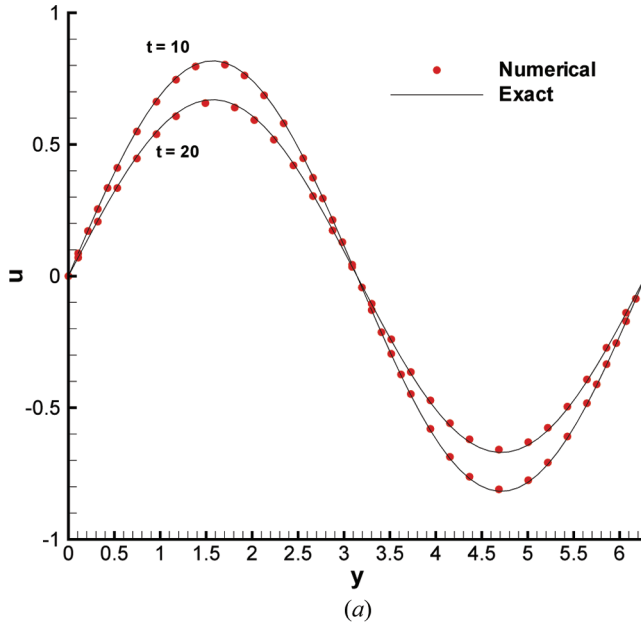
Figure 11. Comparison of predicted and exact mid-plane velocity profiles $u(\pi, y)$ and $v(x, \pi)$ at two different times: (a) $u(\pi, y)$; (b) $v(x, \pi)$ (color figure available online).

The results computed in a mesh of 64×64 uniform grids and at $\Delta t = 0.9\pi/32$ will be presented at $\text{Re} = 100$. Figures 11a and b show a good comparison between the computed and exact u- and v-velocity components at different times along the y- and x-axis lines passing through the centroid of the physical domain.

6.3.2. Doubly periodic shear-layer problem. Subject to the initial conditions $u(x, y \leq 0.5, t = 0) = \tanh[\rho(y - 0.25)], u(x, y > 0.5, t = 0) = \tanh[\rho(0.75 - y)]$, $v(x, y, t = 0) = \bar{\mu} \sin(2\pi x)$, and $p(x, y, t = 0) = 0$, the doubly periodic pair of shear layers will be computed in a unit domain $[0, 1] \times [0, 1]$. In the above, ρ denotes the shear-layer thickness (a larger value of ρ corresponds to a thinner shear layer), and $\bar{\mu}$ denotes the amplitude of the initial perturbation [23].

In this computation, $\bar{\mu} = 0.05$, $\rho = 30$, and $\text{Re} = 10,000$. In Figure 12, the results are plotted with respect to time in 256×256 grids. Figure 13 compares
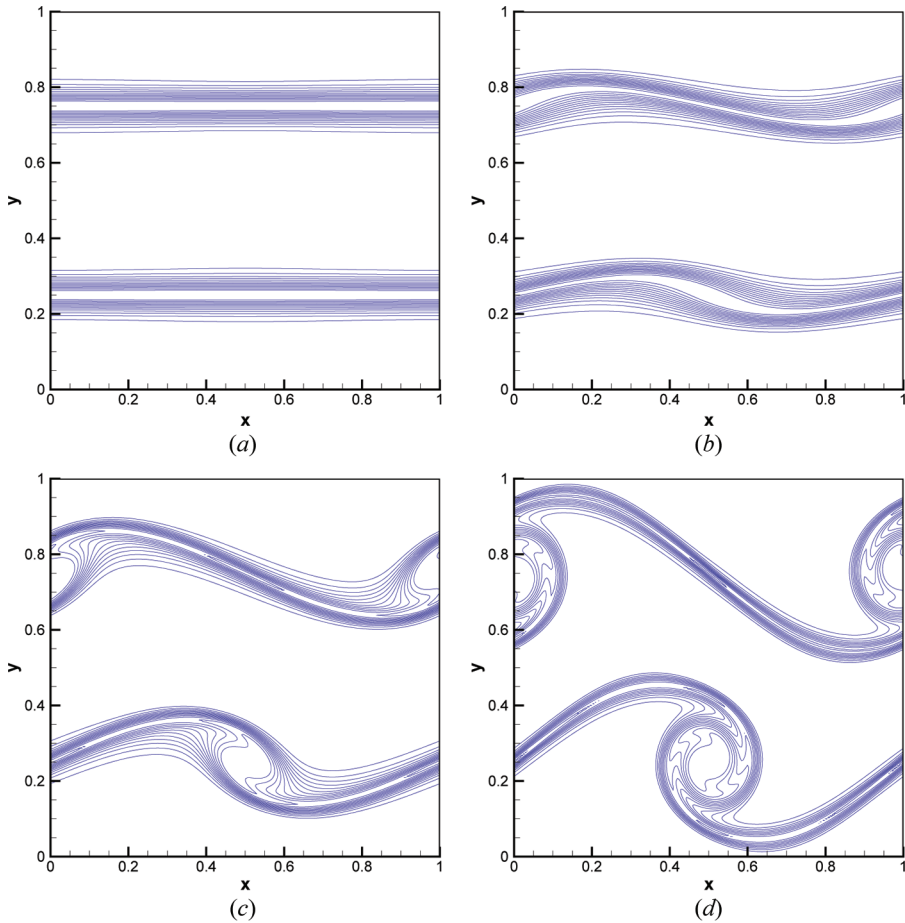
Figure 12. Computed vorticity iso-contours plotted at the four chosen times. The vorticity contour lines are drawn for every 2 dimensionless units. (a) $t = 0$. (b) $t = 0.5$. (c) $t = 0.75$. (d) $t = 1.0$ (color figure available online).
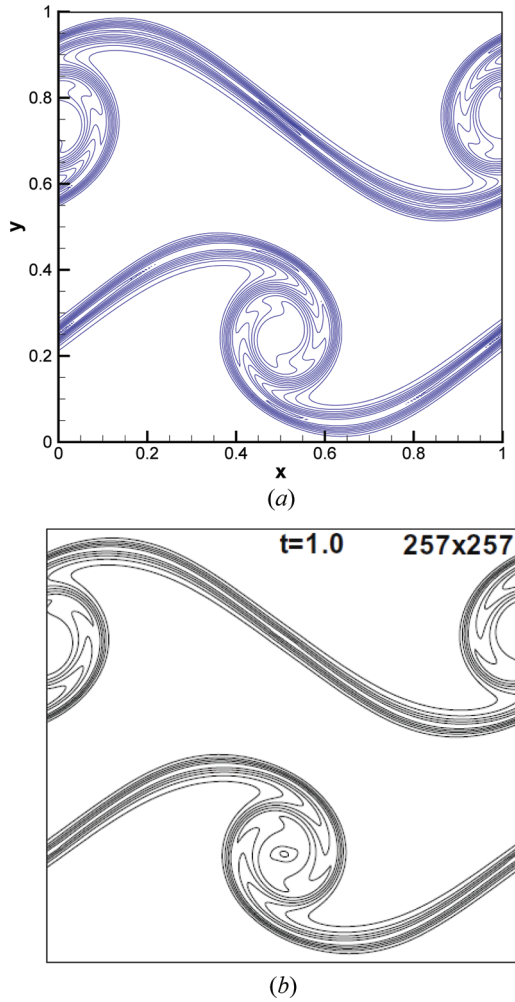
(a)

(b)

Figure 13. Comparison of results predicted from the compact difference scheme [24] and the present scheme at $t = 1$: (a) present; (b) [24] (color figure available online).

the results at $t = 1$ using the present dispersion relation equation–preserving scheme and its non-compact difference scheme given in [24]. Again, the present scheme is shown to give a better result than the non-compact difference scheme.

As for the inviscid case, the vorticity iso-contours are obtained at $\Delta t = 0.01\Delta x$ in a mesh of 256×256 nodal points. At $t = 0, 0.5, 0.75$, and 1.0, the predicted vorticity results are plotted in Figure 14 to exhibit the sharp change of the solution profiles.

In this study we also aim to show that the currently proposed scheme can yield the result that conserves kinetic energy $E\left(= \frac{1}{2}\int_{\Omega} \underline{u} \cdot \underline{u}d\Omega\right)$. The kinetic energy plotted versus time t in Figure 15 remains almost unchanged for the inviscid Euler flow. As
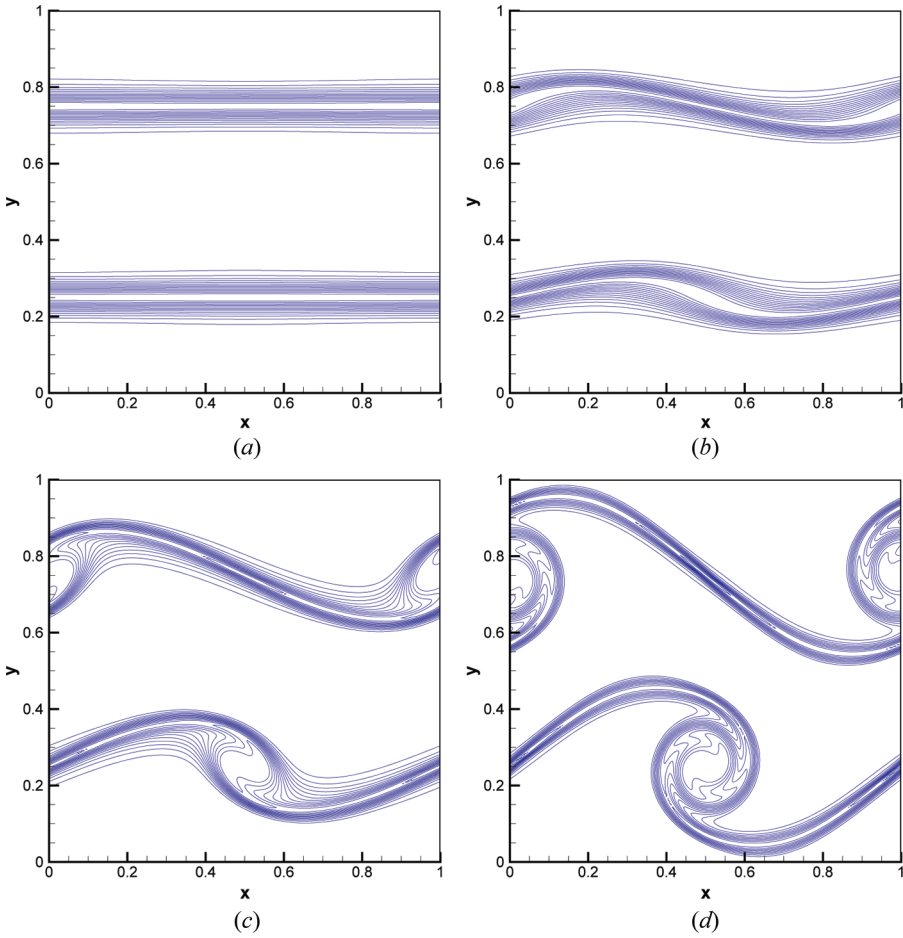
Figure 14. Computed vorticity iso-contours plotted at the four chosen times. The vorticity contour lines are drawn for every 2 dimensionless units: (*a*) $t = 0$. (*b*) $t = 0.5$. (*c*) $t = 0.75$. (*d*) $t = 1.0$ (color figure available online).

for the viscous case, the kinetic energy is no longer conserved and is rather decayed with time, for example, at $Re = 10,000$.

6.4. Two-Phase Flow Problems

In this study the level-set equation given below is applied together with the hydrodynamic equations for an incompressible fluid flow to simulate the time-varying interface (or free surface) [25]:

$$\phi_t + \underline{u} \cdot \nabla\phi = 0 \tag{32}$$
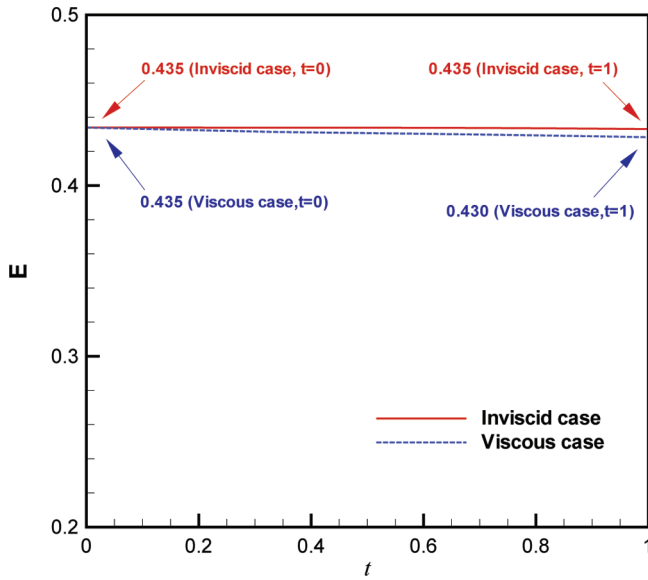
Figure 15. Predicted ratios $E[\equiv E(t)/E(t=0)]$, where E denotes the kinetic energy, plotted with respect to dimensionless time (color figure available online).

In the above, $\underline{u}$ denotes the flow velocity. Along the interface, the value of ϕ is equal to zero. The level-set function ϕ is initially prescribed to have the following set of the signed distance values:
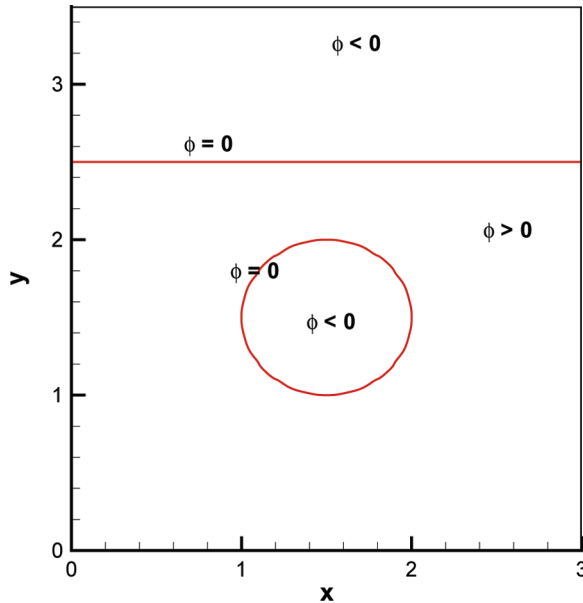

Figure 16. Schematic of the initial condition for the bubble rising problem (color figure available online).

$$\phi = \begin{cases} -d & \text{for } x \in \Omega_{\text{gas}} \\ 0 & \text{for } x \in \Gamma_{\text{free surface}} \\ d & \text{for } x \in \Omega_{\text{liquid}} \end{cases} \tag{33}$$

In the above, d denotes the absolute distance normal to the interface.

Within each time step Δt, the level-set value ϕ will be computed first from Eq. (32), which is normally employed to advect the level-set function ϕ. The computed value of ϕ is then employed as the initial solution to solve the following re-initialization equation so that the level-set value can be always kept as the distance function:

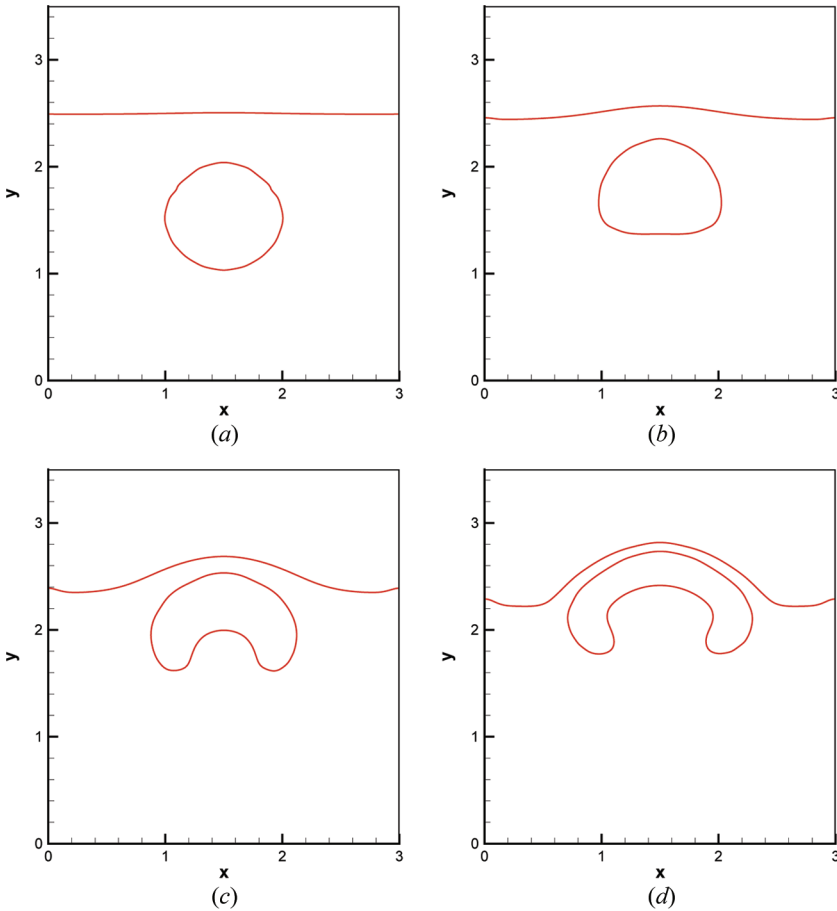$$\phi_\tau + \text{sgn}(\phi_0)(|\nabla\phi| - 1) = \lambda\delta(\phi)|\nabla\phi| \tag{34}$$

Figure 17. Predicted time-evolving free surfaces of the rising bubble at $\text{Re} = 200$: (*a*) $t = 0.5$; (*b*) $t = 1.5$; (*c*) $t = 2.5$; (*d*) $t = 3.5$ (color figure available online).

In the above, $\text{sgn}(\phi_0) = 2\left[H^*(\phi_0) - \frac{1}{2}\right]$ and the smoothed Heaviside function H^* is

$$H^*(\phi) = \begin{cases} 0 & \text{if } \phi < -\varepsilon \\ \frac{1}{2}\left[1 + \frac{\phi}{\varepsilon} + \frac{1}{\pi}\sin\left(\frac{\pi\phi}{\varepsilon}\right)\right] & \text{if } |\phi| \leq \varepsilon \\ 1 & \text{if } \phi > \varepsilon \end{cases} \tag{35}$$

The Dirac delta function $\delta(\phi)$ shown in (34) is approximated by

$$\delta(\phi) = \begin{cases} 0 & \text{if } |\phi| > \varepsilon \\ \frac{1}{2\varepsilon}\left[1 + \cos\left(\frac{\pi\phi}{\varepsilon}\right)\right] & \text{if } |\phi| \leq \varepsilon \end{cases} \tag{36}$$

In this study, the value of ε is chosen as $2\Delta x$ in the following two free-surface problems. To conserve the area enclosed by the interface, λ shown in Eq. (34) is prescribed as follows [26]:
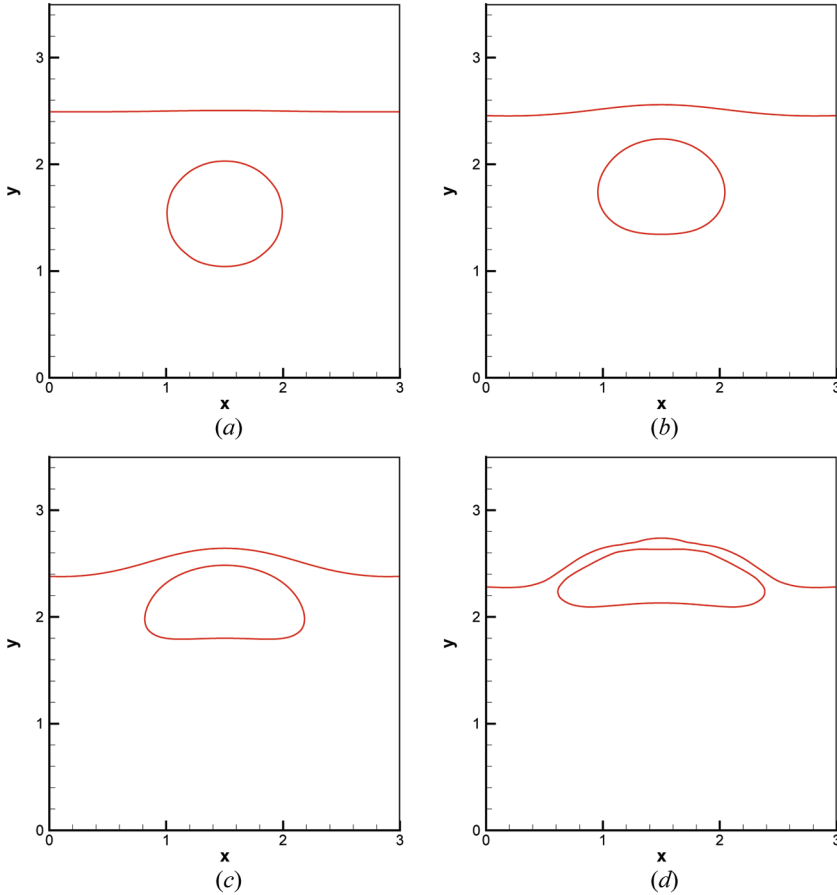

Figure 18. Predicted time-evolving free surfaces of the rising bubble at Re $= 200$ and We $= 10$: (a) $t = 0.5$; (b) $t = 1.5$; (c) $t = 2.5$; (d) $t = 3.5$ (color figure available online).

$$\lambda = -\frac{\int_{\Omega_{i,j}} \delta(\phi)[-\text{sgn}(\phi_0)(|\nabla\phi| - 1)]d\Omega}{\int_{\Omega_{i,j}} \delta^2(\phi)|\nabla\phi|d\Omega} \tag{37}$$

For the two immiscible fluids under investigation, liquid fluid and gas are both assumed to be incompressible. The resulting equations of motion for these fluids can be represented by the following dimensionless continuity equation $\nabla \cdot \underline{u} = 0$ and the incompressible Navier-Stokes equations

$$\underline{u}_t + (\underline{u} \cdot \nabla)\underline{u} = \frac{1}{\rho(\phi)}\left\{-\nabla p + \frac{1}{\text{Re}}\nabla \cdot [2\mu(\phi)\underline{\underline{D}}] - \frac{1}{\text{We}}\delta(\phi)\kappa(\phi)\nabla\phi\right\} + \frac{1}{\text{Fr}^2}\bar{e}_g \tag{38}$$

Equation (38) involves the Reynolds number $\text{Re}(= \rho_r u_r l_r/\mu_r)$, Froude number $\text{Fr}(= u_r/\sqrt{gl_r})$, and Weber number $\text{We}(= \rho_r u_r^2 l_r/\sigma)$. In the above, σ is denoted as the surface tension coefficient and u_r, l_r, ρ_r, μ_r are the referenced values chosen for the normalization of the respective velocity, length, density, and viscosity. The tensor $\underline{\underline{D}}[= \frac{1}{2}(\nabla\underline{u} + \nabla\underline{u}^{\text{T}})]$ shown above denotes the rate of deformation. The curvature of the surface can be theoretically expressed in terms of the level-set function as $\kappa(\phi) = \nabla \cdot \nabla\phi/|\nabla\phi|$.

In each phase, fluid properties may change sharply across the interface. To avoid numerical instability near the interface, the fluid density given by $\rho(\phi) = \rho_L + (\rho_L - \rho_G) H^*(\phi)$ and the viscosity given by $\mu(\phi) = \mu_L + (\mu_L - \mu_G) H^*(\phi)$ are both assumed to vary smoothly across the interface through the use of smoothed Heaviside function $H^*(\phi)$. The subscripts G and L represent the gas and liquid phases, respectively.
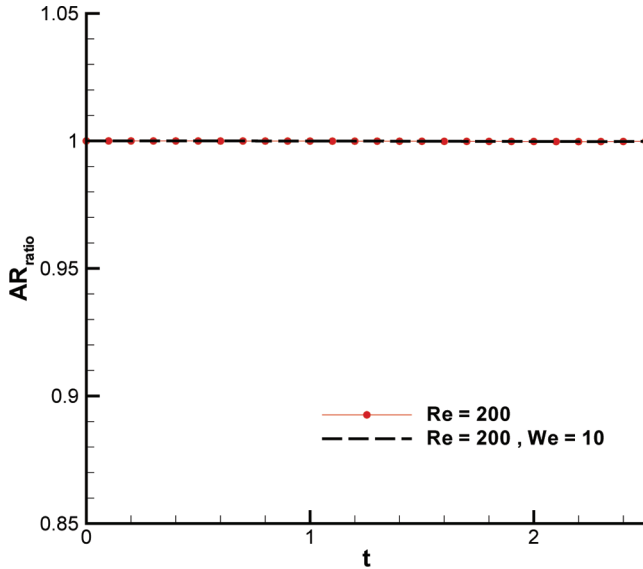

Figure 19. Bubble area ratio AR_{ratio} plotted with respect to time for the cases with/without surface tension effect (color figure available online).

6.4.1. Bubble rising in a partially filled container. The rising buoyant bubbles are studied in the two-dimensional domain [27]. We first consider the case in a rectangular domain $[0, 3.0] \times [0, 3.5]$. Below the free surface, there is a single circular bubble (see Figure 16). The center of the bubble is located at $(1.5, 1.5)$ and its radius is $R = 0.5$. Computation is carried out in the mesh of 180×210 grid points. The density and viscosity ratios are $\rho_l/\rho_g = 2$ and $\mu_l/\mu_g = 2$. The Reynolds number used in the calculation is 200 without taking surface tension into account [27]. In Figure 17, one can see that the investigated bubble gets more deformed as it
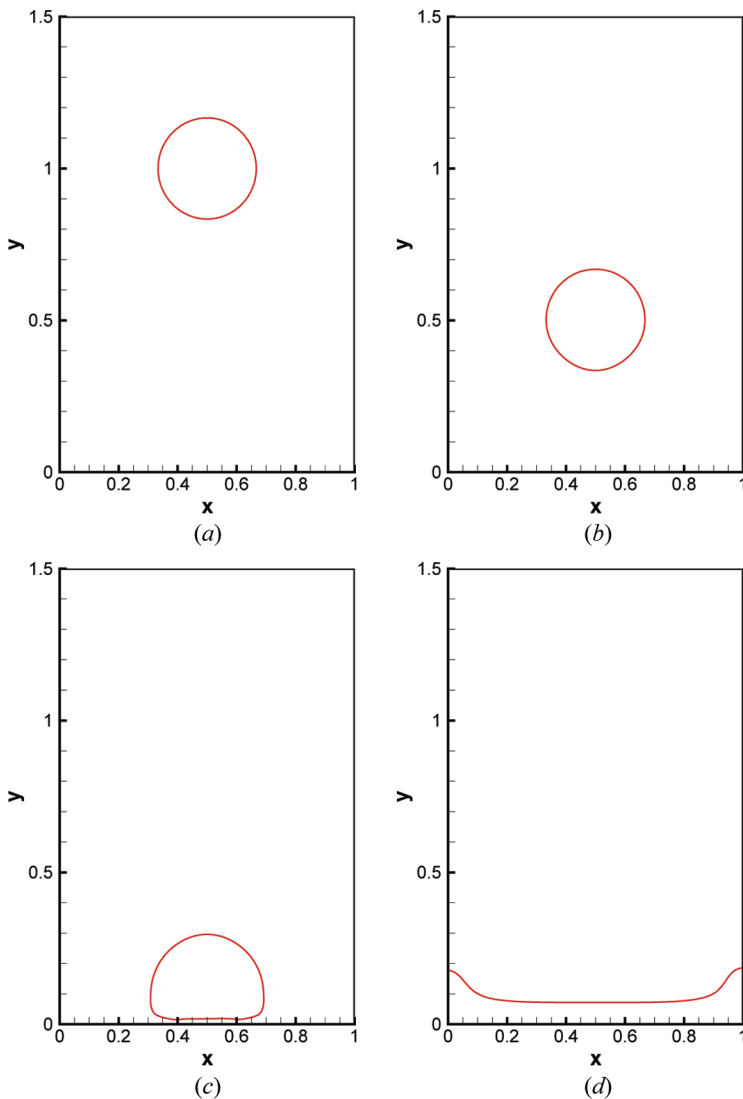

Figure 20. Predicted time-evolving free surfaces of the falling droplet at $\mathrm{Re} = 7{,}787$ and $\mathrm{We} = 550$: (*a*) $t = 0.0$; (*b*) $t = 1.0$; (*c*) $t = 1.33$; (*d*) $t = 2.0$ (color figure available online).
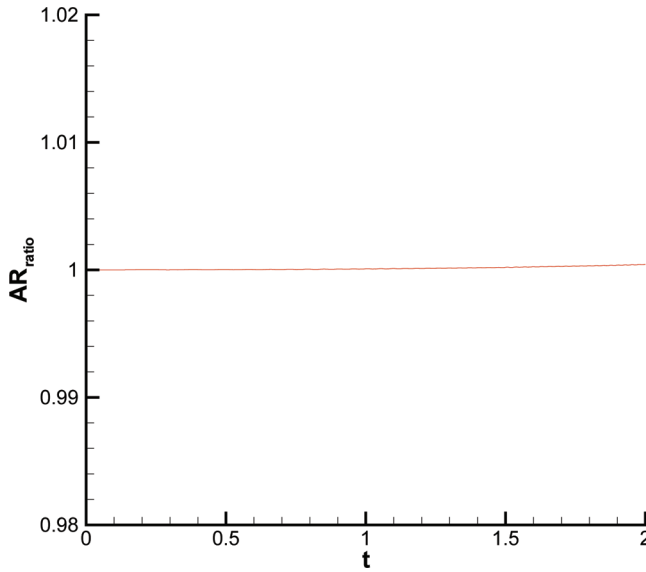
Figure 21. Falling droplet area ratio AR_{ratio} plotted with respect to time (color figure available online).

approaches the surface as time evolves. It is noted that the presently predicted interfaces agree fairly with those predicted in [27].

The time sequence of the rising bubble considered at $Re = 200$ and $We = 10$ is shown in Figure 18. Like the earlier test case, the bubble accelerates from its initial position because of the buoyancy force. No significant difference between the two cases is observed before $t = 1.5$. At a time greater than 1.5, for the cases with/without surface tension the difference becomes apparent, since the effect of surface tension becomes increasingly important. For the sake of completeness, the area ratio $AR_{ratio} = AR(t)/AR(t = 0)$, where $AR(t) = \int_{\phi \geq 0} d\Omega$ [28], is also plotted versus time in Figure 19. It can be seen again that the bubble area is well conserved.

6.4.2. Droplet falling problem. Subject to the gravity field (which is $9.81\,\mathrm{m/s^2}$), a falling liquid droplet is simulated under the effect of surface tension, which is $0.0073\,\mathrm{N/m}$. For this falling droplet problem, the gas viscosity, liquid viscosity, gas density, and liquid density are $1.79 \times 10^{-5}\,\mathrm{kg/m/s}$, $1.137 \times 10^{-3}\,\mathrm{kg/m/s}$, $1.226\,\mathrm{kg/m^3}$, and $1.0 \times 10^3\,\mathrm{kg/m^3}$, respectively. A $2\,\mathrm{cm} \times 3\,\mathrm{cm}$ domain is discretized to yield a uniform mesh of 120×180 grids.

Initially, the bubble center is located at $(1\,\mathrm{cm}, 1\,\mathrm{cm})$ and its radius is $\frac{1}{3}$ cm. No-slip boundary condition is applied along the boundary of the rectangular container. In Figure 20, the predicted free surface is plotted with respect to time for the case taking the surface tension into account. The area ratio AR_{ratio} of the investigated falling droplet is plotted with respect to time in Figure 21. The ability of employing the symplecticity-preserving scheme to conserve the area is numerically confirmed again.

7. CONCLUDING REMARKS

In the light of the Clebsch velocity decomposition theory, the incompressible Navier-Stokes equation is decomposed into the incompressible Euler equation and the time-dependent diffusion equation. The Hamiltonian and Casimir properties embedded in the Euler equation are shown to be retained discretely using the proposed three-step fractional splitting solution algorithm. After a long simulation time, the computed solution still conserves the Hamiltonian and Casimir invariants quite well, implying that the predicted incompressible flow solution is physically correct. In the pure advection solution step, which involves the incompressible Euler equations, two conservation laws are discretely retained by employing the second-order-accurate implicit symplectic Runge-Kutta time integrator. Several benchmark problems have been investigated with great success, and the integrity of applying the newly proposed method is demonstrated.

REFERENCES

1. T. W. H. Sheu and C. H. Yu, Development of an Incompressible Navier-Stokes Solver Involving Symplectic and Non-Symplectic Time Integrators, *Numer. Heat Transfer B*, vol. 58, pp. 262–286, 2010.
2. P. J. Morrison, Hamiltonian Description of the Ideal Fluid, *Rev. Mod. Phys.*, vol. 70, pp. 467–521, 1998.
3. W. Weber, Uber eine Transfornation der hydrodynamischen Gleichungen, *J. Reine. Angew. Math.*, vol. 68, pp. 286–292, 1868.
4. A. J. Chorin, Numerical Solution of the Navier-Stokes Equations, *Math. Comput.*, vol. 22, pp. 745–762, 1968.
5. A. Clebsch, Uber die Integration der hydrodynamischen Gleichungen, *J. Reine. Angew. Math.*, vol. 56, pp. 1–10, 1859.
6. D. Gurarie, Symmetries and Conservation Laws of Two-Dimensional Hydrodynamics, *Phys. D*, vol. 86, pp. 621–636, 1995.
7. T. G. Shepherd, A General Method for Finding Extremal States of Hamiltonian Dynamical Systems, with Applications to Perfect Fluids, *J. Fluid Mech.*, vol. 213, pp. 573–587, 1990.
8. W. Oevel and M. Sofroniou, Symplectic Runge-Kutta Schemes II: Classification of Symmetric Methods, University of Paderborn, Germany, Preprint, 1997.
9. A. Lerat, P. Cinnella, and B. Michel, High-Order Residual-Based Compact Scheme for Aerodynamics and Aeroacoustics, *Comput. Fluids*, vol. 61, pp. 31–38, 2012.
10. J. W. Kim and R. D. Sandberg, Efficient Parallel Computing with a Compact Finite Difference Scheme, *Comput. Fluids*, vol. 58, pp. 70–87, 2012.
11. S. K. Lele, Compact Finite Difference Schemes with Spectral-Like Resolution, *J. Comput. Phys.*, vol. 103, pp. 16–42, 1992.
12. Z.-H. Wan, L. Zhou, and D.-J. Sun, Robustness of the Hybrid DRP-WENO Scheme for Shock Flow Computations, *Int. J. Numer. Meth. Fluids*, vol. 70, pp. 985–1003, 2012.
13. T. K. Sengupta, M. K. Rajpoot, and Y. G. Bhumkar, Space-Time Discretizing Optimal DRP Schemes for Flow and Wave Propagation Problems, *Comput. Fluids*, vol. 47, pp. 144–154, 2011.
14. P. H. Chiu, T. W. H. Sheu, and R. K. Lin, Development of a Dispersion Relation Preserving Upwind Scheme for Incompressible Navier-Stokes Equations on Nonstaggered Grids, *Numer. Hear Transfer B*, vol. 48, pp. 543–569, 2005.

15. T. W. H. Sheu, N. S. C. Kao, P. H. Chiu, and C. S. Lin, Development of an Upwinding Scheme through the Minimization of Modified Wavenumber Error for the Incompressible Navier-Stokes Equations, *Numer. Hear Transfer B*, vol. 60, pp. 179–202, 2011.

16. C. Cheong and S. Leey, Grid-Optimized Dispersion-Relation-Preserving Scheme on General Geometries for Computional Aeroacoustics, *J. Comput. Phys.*, vol. 174, pp. 248–276, 2001.

17. P. C. Chu and C. Fan, A Three-Point Combined Compact Difference Scheme, *J. Comput. Phys.*, vol. 140, pp. 370–399, 1998.

18. J. von Neumann and R. D. Richtmyer, A Method for the Numerical Calculation on Hydrodynamic Shocks, *J. Appl. Phys.*, vol. 21, pp. 232–237, 1950.

19. S. T. Zalesak, Fully Multidimensional Flux Corrected Transport Algorithms for Fluids, *J. Comput. Phys.*, vol. 31, pp. 335–362, 1979.

20. P. Tamamidis and D. N. Assanis, Evaluation of Various High-Order-Accuracy Schemes with and without Flux Limiters, *Int. J. Numer. Meth. Fluids*, vol. 16, pp. 931–948, 1993.

21. A. Ghods, F. Sobouti, and J. Arkani-Hamed, An Improved Second Moment Method for Solution of Pure Advection Problems, *Int. J. Numer. Meth. Fluids*, vol. 32, pp. 959–977, 2000.

22. A. Quarteroni, F. Saleri, and A. Veneziani, Factorization Methods for the Numerical Approximation of Navier-Stokes Equations, *Comput. Meth. Appl. Mech. Eng.*, vol. 188, pp. 505–526, 2000.

23. A. Shah, L. Yuan, and A. Khan, Upwind Compact Finite Difference Scheme for Time-Accurate Solution of the Incompressible Navier-Stokes Equations, *Appl. Math. Comput.*, vol. 215, pp. 3201–3213, 2010.

24. M. L. Minion and D. Brown, Performance of Under-resolved Two-Dimensional Incompressible Flow Simulation: II, *J. Comput. Phys.*, vol. 138, pp. 734–765, 1997.

25. S. Osher and J. A. Sethian, Fronts Propagating with Curvature-Dependent Speed: Algorithms Based on Hamilton-Jacobi Formulations, *J. Comput. Phys.*, vol. 79, pp. 12–49, 1988.

26. S. Osher and R. Fedkiw, *Level Set Methods and Dynamic Implicit Surfaces*, Springer-Verlag, Berlin, 2003.

27. Y. Zhao, H. H. Tan, and B. Zhang, A High-Resolution Characteristics-Based Implicit Dual Time-Stepping VOF Method for Free Surface Flow Simulation on Unstructured Grids, *J. Comput. Phys.*, vol. 183, pp. 233–273, 2002.

28. R. I. McLachlan, Area Preservation in Computational Fluid Dynamics, *Phys. Let. A*, vol. 264, pp. 36–44, 1999.